



ASME Journal of Applied Mechanics Online journal at:

https://asmedigitalcollection.asme.org/appliedmechanics



Thomas Vitalis

Department of Civil & Environmental Engineering, University of Massachusetts Amherst, Amherst, MA 01003 e-mail: tvitalis@umass.edu

Andrew Gross

Department of Mechanical Engineering, University of South Carolina, Columbia, SC 29208 e-mail: andrewgross@sc.edu

Simos Gerasimidis¹

Department of Civil & Environmental Engineering, University of Massachusetts Amherst, Amherst, MA 01003 e-mail: sgerasimidis@umass.edu

Mechanical Response and Failure Modes of Three-**Dimensional Auxetic Re-Entrant LPBF-Manufactured Steel Truss Lattice Materials**

Auxetic architected materials present a novel class of damage-tolerant materials with tunable mechanical characteristics and high energy absorption due to their unique ability to laterally contract and densify when subjected to axial compressive loading. The current state of research on negative Poisson's ratio materials mainly focuses on 2D geometries and a few families of 3D geometries with limited experimental comparisons between different architectures and various geometrical features. Furthermore, when manufactured via laser powder bed fusion, the influence of as-built deviations of geometrical and material properties inherently present due to the melt pool solidification process for thin features is relatively unexplored in the case of metal-architected materials. The authors aim to study the elastic properties, peak characteristics, and failure modes of steel auxetic truss lattices subjected to axial compression while also addressing the uncertainties inherent to the metal laser powder bed fusion additive manufacturing of architected materials. This work presents an experimental and computational exploration and comparison of two promising three-dimensional auxetic truss lattice families of low relative densities. A comprehensive investigation of metal negative Poisson's ratio mechanical metamaterials is presented, including the selection of the architectures, modeling, laser powder bed fusion additive manufacturing, as-built part characterization, material testing, and mechanical testing under axial compression. The study of such architectures can unlock their potential in making them readily adaptable to a wide variety of engineering applications.

[DOI: 10.1115/1.4065669]

Keywords: elasticity, mechanical properties of materials, plasticity, stress analysis, structures

1 Introduction

The recent advances in additive manufacturing methods have stimulated the interest of engineers, physicists, and materials scientists to design, model, and manufacture new types of truss lattice materials, enabling the design of materials with behavior that is otherwise inaccessible. New emerging classes of stochastic and nonstochastic lattice materials with extraordinary mechanical properties that haven't been observed in naturally occurring materials are opening new horizons for aerospace [1], defense [2,3], soft robotics and sensor-development [4], compliant materials [5], civil infrastructure [6-8], high-energy absorption materials [9,10], and biomedical applications [11]. These materials are often referred to as metamaterials in the literature. Even though developing an understanding of such cellular solid materials has been a topic of discussion since the late 1980s from the authors [12–17], the widespread adoption of additive manufacturing for rapid prototyping has bolstered the growth of the field and given birth to ideas such as multiscale materials [18], novel composites [19,20], tunable bandgap materials [21], viscoelastic solids [22], and hierarchical metamaterials [23-26].

Auxetic or negative Poisson's ratio materials have been at the forefront of developing novel truss lattice architected materials since they are highly tunable and can achieve superior indentation resistance, high stiffness, and high specific energy absorption [12-14,27,28], compared to convex architectures. Pronounced lateral contraction of the material gives rise to their ability to selfdensify when subjected to compressive stress or indentation loading (auxeticity). This actuation effect is generated due to the re-entrant characteristic angles that form many geometric motifs,

¹Corresponding authors.

Contributed by the Applied Mechanics Division of ASME for publication in the JOURNAL OF APPLIED MECHANICS. Manuscript received February 9, 2024; final manuscript received May 28, 2024; published online July 5, 2024. Assoc. Editor: Pradeep

which, under axial compression, induce bending-dominated strains in the truss lattices. Even though two-dimensional planar auxetic structures have been thoroughly studied both analytically and experimentally due to the fabrication ease and low manufacturing cost of experimental specimens [29–34], three-dimensional auxetic families have been a topic of relatively limited experimental exploration [10,28,35–38]. Furthermore, the influence of using a ductile or brittle bulk material for three-dimensional experimental lattices can alter the mechanical behavior of the specimens by allowing different degrees of geometric non-linearities [18].

Researchers have demonstrated a range of different techniques for manufacturing truss lattice architected materials [39]. The selection of the bulk solid material and the manufacturing technique are heavily dependent on the feature size of the specimen and the available equipment. Typically additively manufactured truss lattices possess feature sizes ranging from the nanometer scale to the micrometer scale [40–42] and millimeter scale [6,11,18], feature sizes that are suitable for a variety of additive manufacturing techniques such as selective laser melting, directed energy deposition, and electron beam melting [43]. Typically, laser powder bed fusion metal 3D-printing methods induce unavoidable stochastic features [44,45] and spatial variation on the final parts due to the physics involved in the melt pool solidification process [46–50].

Even though metal auxetic three-dimensional truss lattices have been studied in numerous publications [36,51–60], there is only little comparable experimental information on different characteristic angles of three-dimensional architectures and studies that can effectively compare two different architectural families, while particularly focusing in their failure behavior. Experimental results of various geometrical configurations of auxetics are imperative to understanding the mechanical behavior of three-dimensional auxetic truss lattices, as well as the various mechanical behaviors that arise in the elastic and plastic regimes. Furthermore, characterization of the as-built metal architected materials is critical in achieving accurate numerical predictions [46,61] for the capacity of architected truss lattices.

In this paper, we report findings on the compressive behavior of two families of steel auxetic truss lattice architectures, specifically focusing on the elastic properties, peak stresses, Poisson's ratios, and deformation modes of these architectures. The laser powder bed fusion additive manufacturing method is employed with the use of a 15-5 precipitation hardening stainless steel alloy, concentrating on the anisotropy and spatial variation of the produced parts. The deliberate selection of the millimeter scale of the study was driven by its adaptability for creating diverse prototypes related to civil infrastructure, such as interpenetrating phase composites of truss lattice-reinforced concrete structural elements. The study of such functional prototypes in this scale can inform the fundamental mechanics involved in architected materials and architected material composites and enable their upscaling for use in civil infrastructure structural elements and other engineering applications. First, the fabrication of auxetic truss lattices with a stainless steel alloy is discussed using the laser powder bed fusion (LPBF) method, and the challenges involved in the design for additive manufacturing (dfAM) are delineated. Second, we present findings on the physical and mechanical properties of the manufactured specimens by employing in situ characterization techniques. The discussion delves into the inherent anisotropy of as-built parts with thin features. An analysis of the spatial variability that occurs during the melt pool solidification process in architected truss lattice parts is presented. The compressive characteristics of steel auxetic truss lattices from two distinct geometric families with different elastic moduli and Poisson's ratio are assessed experimentally. A computational validation of the experiments is performed by leveraging material properties obtained through characterization techniques, such as μ CT and scanning electrode microscopy (SEM). By using the same model definition that described the behavior of the experimental specimens, results for truss lattices with varying relative densities, and the effect of relative density on the compressive properties is analyzed. Overall, this work aims to provide a better understanding of the mechanical behavior of two threedimensional steel auxetic re-entrant families while quantitatively characterizing the as-built specimens and discussing the LPBF-induced imperfections that occur during the manufacturing process.

2 Explorative Finite Element Computations

The literature on auxetic materials provide an abundance of auxetic truss lattice unit cells [9,56,62-72]. A vast range of threedimensional unit cells was initially considered by the authors, with manufacturability and effective Poisson's ratios in mind. During the selection process, the architectures characterized by reduced intricacy and nodal connectivities (Z) were deemed as advantageous candidates for further investigation due to their compatibility with novel civil infrastructure applications [6,7,8]. Two of the re-entrant families exhibiting some of the lowest Poisson's ratios were selected: the auxetic bowtie honeycomb geometry (BT) and the auxetic double pyramid geometry (DP) (Fig. 1). These architectures demonstrate a similar range of nodal connectivities (Z=5 for BTs, Z = 5.333 for DPs) but substantial variations in predicted auxeticity (ν) , and axial/transverse moduli $(E_3, E_1 = E_2)$, depending on the specifics of their geometry, that consequently make them more or less compliant at equal relative densities ρ^* .

The mechanical properties of an architected material are mainly governed by the relative density ρ^* of the material and by the architecture [12]. To determine a set of desirable geometrical features (characteristic angles), the bowtie and double pyramid architectures were parameterized by key angles in their design. The bowtie has one such angle θ , which was varied in steps of 5 deg from θ = 70 deg to 135 deg to generate re-entrant and convex lattices. The double pyramid has two relevant angles. The first θ_1 was varied in steps of 5 deg from θ_1 = 10 deg to 60 deg. The second angle θ_2 varied between a lower bound near 0 and an upper bound of θ_2 = 180 deg $-2\theta_1$, with at least ten steps in-between. The relative density of all designs was kept constant at ρ_{UC}^* = 5% to minimize

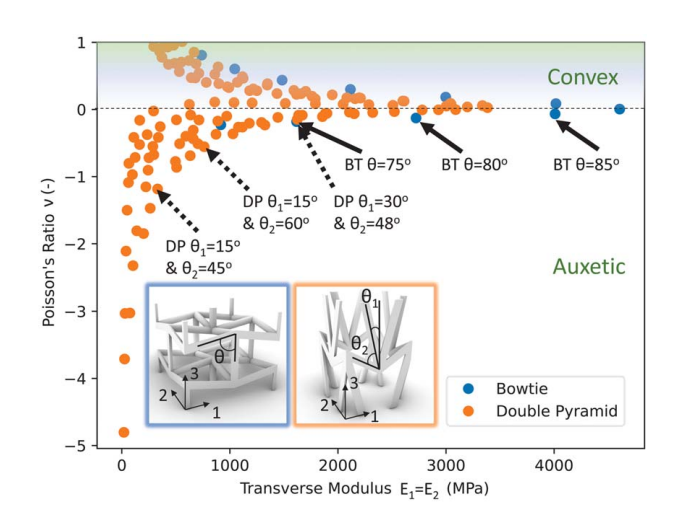


Fig. 1 FEA computations of the Poisson's ratio $\nu_{31}=\nu_{32}$ and transverse moduli $E_1=E_2$ for both bowtie and double pyramid geometries, with periodic boundary conditions. The double pyramid architectures can achieve lower Poisson's ratios and increased compliance compared to the bowtie architectures. The presence of a second characteristic angle in the double pyramids provides greater tunability of their elastic properties in the design space. The bowtie with $\theta=90$ deg exhibits a $\nu_{31}=0$, and every convex honeycomb geometry (characteristic angle higher than $\theta>90$ deg) generates positive Poisson's ratio. Similarly, certain double pyramid θ_1 and θ_2 combinations result in positive Poisson's ratio.

the impact of relative density on differences found between the properties of the various geometries.

The BT and DP unit cells were analyzed with the commercially available finite element analysis (FEA) package ABAQUS/STANDARD (Dassault Systémes, Johnston, RI) [73]. The models used approximately 50,000-500,000 tetrahedral elements (depending on the geometry) with quadratic shape functions (C3D10). Periodic boundary conditions were applied with a PYTHON script to obtain results free of edge effects. The use of periodic boundary conditions allows for efficient simulation of truss lattice materials prior the occurrence of deformation modes deviate from periodicity (e.g., localization of deformation or fracture). The nine required elastic constants for orthotropic materials were calculated following the simulation procedure outlined in Ref. [74]. These simulations assumed small deformations and linear material behavior, where available material properties were obtained from the metal powder alloy specification sheet that is presented later in Sec. 3.1 (Table 2) and unavailable material properties from the alloy manufacturer were assigned the typical values for steel $E = 200 \,\text{GPa}$, $\nu = 0.30$.

The results of this analysis have shown that the double pyramid architecture can produce more laterally compliant unit cells that achieve lower Poisson's ratios when compared to the bowtie geometry (Fig. 1). Unit cells that exhibit similar Poisson's ratio and transverse moduli illustrate different axial moduli and unit cell aspect ratios between the two families, such as the double pyramid $\theta_1 = 30 \text{ deg}$ and $\theta_2 = 48 \text{ deg}$ and bowtie $\theta = 75 \text{ deg}$ architectures (Figs. 1 and 2). Additionally, it is observed that geometries with a Poisson's ratio $\nu_{31} \approx 0$ exhibit the largest transverse modulus (Fig. 2).

Three geometric configurations from each auxetic family were selected based on a combination of the minimum achievable Poisson's ratio ν_{31} and the range of the transverse modulus E_1 . A set of truss lattice designs that cover a large range in the tradeoff between these properties was selected to explore their compressive behavior when subjected to large compressive strains. The designs that achieved a wide range of mechanical properties in the periodic boundary condition computations are the $\theta = 75 \deg$, $\theta = 80 \deg$,

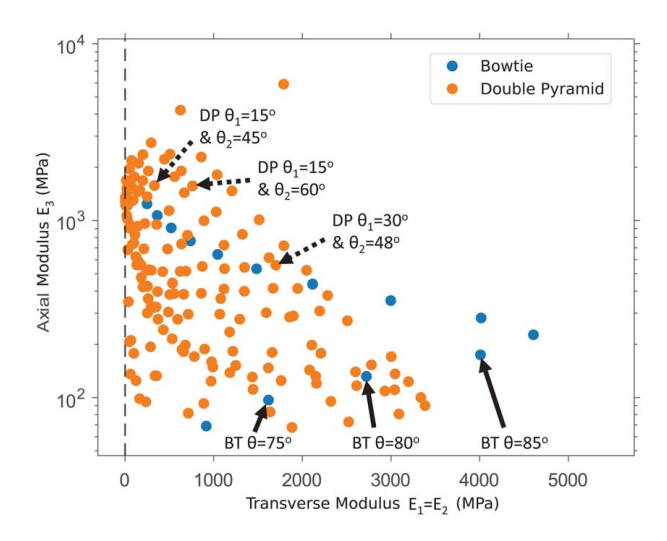


Fig. 2 FEA computations of the transverse moduli $E_1=E_2$ plotted against axial moduli E_3 (log scale) for both bowtie and double pyramid architectures, with periodic boundary conditions. The largest transverse moduli in each family are found for designs with $\nu_{31}\approx 0$. A wide range of axial moduli is achieved by altering the characteristic angles of both architectures. In the case of the double pyramids, an abundance of designs illustrates very low values of $E_1=E_2$, thus exhibiting substantially increased lateral compliance. Convex honeycomb geometries present increased axial moduli compared to the auxetic bowties, while still accomplishing a wide range of transverse moduli.

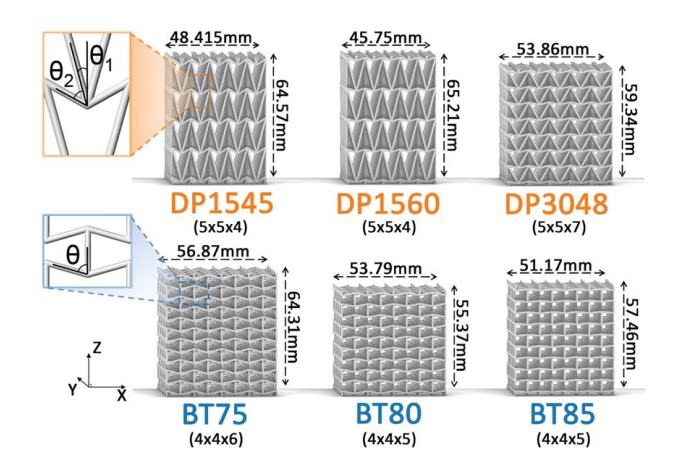


Fig. 3 Renders of the selected geometric configurations from the periodic BC computations, arranged in the nearest possible tessellations approaching a 2 in. cube design. The characteristic angles of each architecture and tessellation dimensions are shown, along with the universal coordinate system pertaining to the build directions. The specifics of each architecture are presented in more depth in Table 1. The unit cell relative density is kept constant at $\rho_{UC}^*=5\%$, while the tessellation relative density presents small fluctuations (Table 1). The tessellations are tetragonal so that the Y-dimension is equal to the X-dimension.

and $\theta=85\,\mathrm{deg}$ for the one-angle, three-dimensional auxetic bowtie honeycomb family. Similarly, the $\theta_1=15\,\mathrm{deg}$ and $\theta_2=45\,\mathrm{deg}$; $\theta_1=15\,\mathrm{deg}$ and $\theta_2=60\,\mathrm{deg}$; and $\theta_1=30\,\mathrm{deg}$ and $\theta_2=48\,\mathrm{deg}$ were selected for the two-angle three-dimensional double pyramid family designs. These architectures are located at the lowest Poisson's ratio curve and attain a wide range of transverse moduli (Fig. 1). The geometric definitions of the selected candidate architectures are presented in Fig. 3.

3 Materials and Methods

3.1 Manufacturing. To investigate the compressive behavior of the two different auxetic families with $\rho_{UC}^* = 5\%$, laser powder bed fusion was selected as the manufacturing method due to its ability to produce high-quality metal parts that can be readily adopted for various applications or with minimal part post-treatment. A total of nine steel auxetic truss lattice specimens with 1 mm circular strut diameters are manufactured and tested under axial compression to determine the elastic properties, the Poisson's ratios, and their distinct failure modes. We also report findings on the significant manufacturing challenges resulting from the LPBF process that affect the end quality of the part.

The rationale behind the selection of the tessellation sizes was to keep the dimensions as close as possible to the $50.8 \times 50.8 \times 50.8$ mm $(2 \times 2 \times 2 \text{ in.})$ ASTM C109/C109M [6,75] cube while maintaining the unit cell relative density constant at 5%. This set of parameters is aimed at maximizing the per-base plate throughput and maintaining workable dimensions for the experimental setup. These dimensions are also compatible with the manufacturing of mortar/steel interpenetrating phase composites [6]. The design of the dimensions holds particular significance in the case of composite specimen manufacturing due to its close resemblance to the standardized testing of bulk materials. A minimum of four stacked unit cells was used in every direction of the tessellation to minimize edge effects. Additionally, it should be noted that when designing a finite-sized tessellation of the unit cells, slight deviations between the unit cell relative density ho_{UC}^* and the effective density of finite-sized tessellation exist due to edge effects. The circular strut diameters of the tessellations are designed constant at 1 mm to avoid manufacturability issues and severe defects due to

Table 1 Detailed geometric properties of selected architecture tessellations with $\rho_{\text{UC}}^* = 5\%$, as-designed in the CAD software

	Long strut length (mm)	Short strut length (mm)	Unit cell dimensions (mm)	Unit cell volume (mm ³)	Tessellation dimensions (mm)	Truss volume (mm ³)	RD (%)
BT 75 $(4 \times 4 \times 6)$	7.23	NA	$13.97 \times 13.97 \times 10.72$	104.45	56.87 × 56.87 × 64.31	11,624	5.59
BT 80 $(4 \times 4 \times 5)$	6.70	NA	$13.2 \times 13.2 \times 11.07$	96.46	$53.79 \times 53.79 \times 55.37$	8994	5.59
BT 85 $(4 \times 4 \times 5)$	6.30	NA	$12.54 \times 12.54 \times 11.49$	90.36	$51.17 \times 51.17 \times 57.46$	8387	5.57
DP 15-45 $(5 \times 5 \times 4)$	18.32	5.475	$9.48 \times 9.48 \times 14.96$	67.26	$48.415 \times 48.415 \times 64.57$	9153	6.05
DP 15-60 $(5 \times 5 \times 4)$	17.29	4.63	$8.95 \times 8.95 \times 15.50$	62.10	$45.75 \times 45.75 \times 65.21$	8161	5.98
DP 30–48 $(5 \times 5 \times 7)$	10.57	5.40	$10.57 \times 10.57 \times 8.03$	44.93	$53.86 \times 53.86 \times 59.34$	10,303	5.99

Note: The tessellation sizes (Fig. 3) are displayed under the name of each architecture. Unit cells of both architectures are tetragonal, with the bowtie architecture having equal strut lengths inside of a tessellation, with the top and bottom ends being half of that length to maintain periodicity. The double pyramid architectures have two lengths of struts, where the set of struts that more closely align with the Z-direction are longer than the other set.

the melt pool solidification and cutting processes. Owing to the different sizes of tetragonal unit cells that occurred with the changing of the geometrical features of the finite-sized truss lattices, different tessellation sizes were designed for each architecture (Table 1). For all double pyramid architectures, short stubs (1 mm height) were added at the top and bottom of the geometry to assist the lateral actuation of the boundary unit cells without the stubs themselves being too slender, thus avoiding localized buckling. After the selection of the architectures of interest, computer-aided design (CAD) of finite-sized truss lattices ensued. The RHINO 7/PYTHON API (Robert McNeel and Associates, Seattle, WA) [76] was used for the parametric CAD modeling of the finite truss lattices. Additional post-processing of the geometries to prepare the STL files for additive manufacturing was performed in SOLIDWORKS 2022 (Dassault Systémes) [77]. Support generation and base plate preparation for LPBF were performed using MAGICS (Materialise NV, Plymouth, MI) [78].

Preliminary testing of support schemes has shown that cone supports (Fig. 4) had a lower rate of support failures compared to grid supports, while also assisting powder retention and reuse due to their open shape. Additional small block supports were added at the bottom to provide enhanced support at the early manufacturing stages. To provide lateral support for the generated features, 1 mm thin plates were used to surround part of the geometry, and the cutting tolerances were introduced in the form of additional pads between the plates and struts. All parts were oriented -45 deg around both X and Y axes (Fig. 3) to avoid horizontal overhangs in struts, with the exception of the DP1545 architecture that was rotated by an additional -10 deg around the X-axis for the same reason. Finally, slicing and exposure modification took place in

the EOSPRINT 2.0 (EOS GmbH, Novi, MI) software [79]. During manufacturing, a carbon fiber brush recoater was used to reduce lead time and increase the ability to construct larger aspect ratio overhangs inside truss lattices by reducing the forces thin features experience during powder recoating. Cutting the lattices from the build plate and the supports was performed using a Kunshan Ruijun Ltd. (Suzhou, China) FR600 Wire EDM cutter with a 0.2 mm molybdenum wire.

The metal 3D printer used in this study was the EOS M290 (EOS GmbH). The bulk material powder selected for this study was the EOS GmbH 15-5 PH1 pre-alloyed stainless steel in powder form. According to the manufacturer of the powder, 0.5% of the grains are >63 um. The powder's chemistry conforms to DIN 1.4540 and UNS S15500, with approx. 15% of Cr and 5% of Ni and part density of ~ 7.7 g/cm³. The alloy selection was motivated by its excellent mechanical properties, including hardness and strength for a wide variety of engineering applications (Table 2), its corrosion resistance, its heat-treatment ability, and the relatively unexplored material properties in the literature when compared to similar counterparts such as stainless steel 17-4 PH.

Before proceeding with the manufacturing of the truss lattice tessellations shown in Table 1, a series of test unit cells (84 total) were manufactured with a range of exposure settings to assess the feasibility and quality of the exposure scheme. The layer recoating thickness is known to be the main parameter that linearly affects the manufacturing time. To speed up the process and reduce the cost, 40 um and 50 um layer recoating thicknesses were tested and compared to the manufacturer-recommended value of 20 um. For the feasibility study, two sets of laser speeds of 1000 mm/s and 1300 mm/s were used, as well as laser power increments in the range

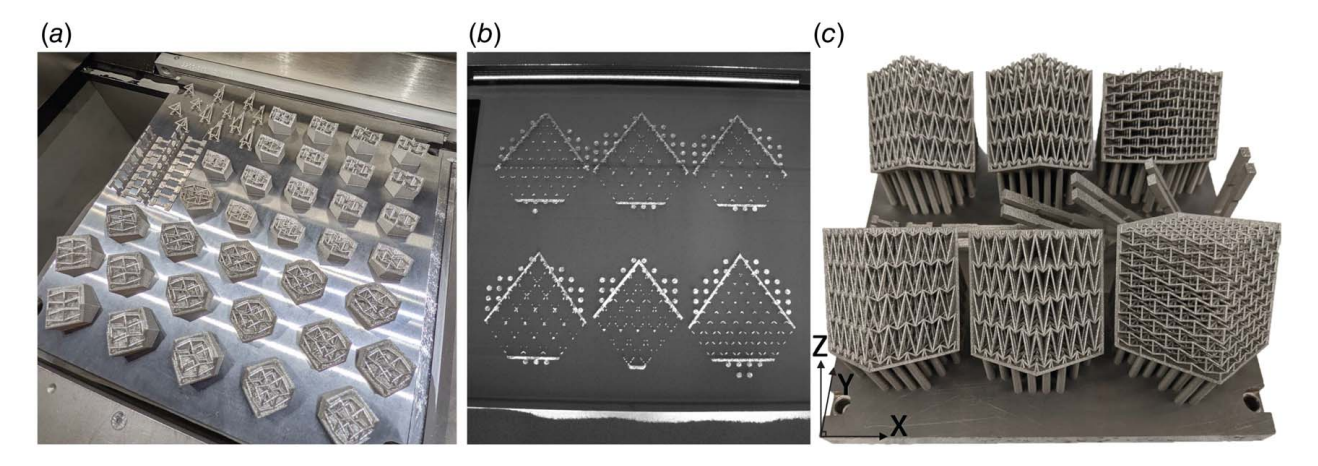


Fig. 4 The LPBF manufacturing process: (a) preliminary manufacturing tests of unit cells during the printing feasibility study rotated 45 deg in both X and Y axes (Fig. 3), to determine tentative exposure profiles, (b) post-exposure snapshot of the powder bed before the recoater spreads another powder layer, and (c) post-cleaning base plate with rotated architectures and material testing coupons. Wire EDM cutting of the parts follows this stage.

Table 2 15-5 PH stainless steel powder specification sheet from the powder manufacturer for a 20 um layer recoating thickness

	UTS (MPa)	Yield stress (MPa)	Elongation at fracture (%)
ZY	1200 ± 50 1200 ± 50	1025 ± 85 930 ± 75	17 ± 4 14 ± 4

Note: XY plane refers to horizontal prints, and Z plane refers to vertical prints. Data on the E and ν are not provided by the manufacturer.

of [195 - 370 W] with 20 W increments. This set yields volumetric energy densities (VEDs) in the range of $[55.56 - 102.78 \text{ J/mm}^3]$ according to Eq. (1), where p is the laser power, v is the laser speed, h is the hatch distance, and t is the laser recoating thickness.

$$VED = \frac{p}{vht} \tag{1}$$

VEDs outside of this range weren't considered in order to avoid keyhole porosity and lack of fusion pores in the alloy microstructure. The hatch distance h was kept constant at $0.09\,\mathrm{mm}$. Two sets of upskin, down skin, and contour configurations were attempted. The first was matching the default VED values for 15-5 PH1 (Supplementary Table 1 available in the Supplemental Materials on the ASME Digital Collection), and the second one was ×0.8 of the default VED settings, with the latter being favored. Even though VED is an appropriate indicator of the laser energy deposited at the powder bed, the quality of the as-built part doesn't translate linearly for the same amount of VED. During manufacturing, parts with the same VED for 20 um and 40 um were visibly overexposed in the case of 40 um. The exposure parameters closer to the center of the range of VEDs that produced visually successful printed parts without noticeable imperfections and artifacts were selected (Table 3) and validated by μ CT porosity measurements presented later on. The overall manufacturing process speed-up gained by using the proposed exposure scheme was approx. 65% compared to the manufacturer's default exposure scheme (Supplementary Table 1).

3.2 As-Built Part Characterization. To study the deviation of the as-built part from the CAD geometry and the effect of this deviation at the as-built part relative densities, micro-computed tomography imaging (μ CT) was performed at the printed finite-sized truss lattices. First, the deviation mechanisms (imperfections) were delineated by using scanning electron microscopy imaging on an unpolished unit cell with uniform 1.2 mm strut diameters, using an FEI Magellan 400 XHR-SEM (Thermo Fisher Scientific Inc., Waltham, MA). The default exposure parameters (Supplementary Table 1 available in the Supplemental Materials on the ASME Digital Collection) were used on a bowtie unit cell laying flat on the base plate substrate with horizontal overhangs to study the quality of a fully vertical print and the worst case of overhangs. An intermediate compromise in the as-built quality of overhangs situated between the vertical and horizontal orientations is anticipated,

particularly in terms of surface roughness, curvature deviations, observed porosity, and the presence of unmelt particles. The manufacturing deviations can be summarized in four categories: (1) strut diameter variation (region A on the upper right of Fig. 5), (2) strut curvature variations (waviness) (region A on the upper right of Fig. 5), (3) partially melt and unmelt powder particles attached to the molten substrate (upper right and lower left of Fig. 5), and (4) internal (closed) and external (open) microstructure porosity (regions B and C on the upper right and lower right of Fig. 5) [46]. The amount and intensity of imperfections were observed to be significantly affected by the overhang angles [47]. The presence of such geometrical imperfections can be detrimental to both the achieved peak stresses and the elastic properties of the as-built truss lattice [80].

X-ray computed tomography was conducted on the manufactured specimens using the ZEISS Xradia 620 Versa (Carl Zeiss AG, Maple Grove, MN) at MIT.nano to characterize the as-built microstructure and part deviation further. Data post-processing were conducted using the DRAGONFLY PRO (Object Research Systems Inc., Montréal, Québec, Canada) [81] software. The porosity of a unit cell was measured to observe imperfections during the melt pool solidification process and additionally provide metrics on the effective diameter distributions inside the truss lattices (ignoring the effects of the boundary wire electrical discharge machining (WEDM) cuts) that consequentially affect the achieved peak stresses. To achieve this, a high-magnification (porosity) scan was performed on the BT75 architecture using a voxel size of $10.2202 \,\mu\text{m}$, and six low-magnification (diameter) scans were performed using a voxel size of $54.09 \,\mu\text{m}$, one for each architecture. An HE18 filter was used for all scans. The X-ray source was set at 160 kV, 25 W, and the still exposure time was 1.2 s to achieve satisfactory X-ray penetration. Due to the large density contrast between air and stainless steel, the acquired dataset was effectively binary after reconstruction. To cancel out the effect of partially filled boundary voxels that exist due to the high surface roughness in the low-magnification scan, the diameter distributions were calibrated using the high magnification scan distributions (Fig. 6). The larger than 10.22 um porosity was minimal and measured at 0.01%, in par with the literature [47]. The porosity metrics were derived from a unit cell scan in the center of the bowtie θ = 75 deg $4 \times 4 \times 6$ architecture. The number of pores is significantly reduced for equivalent spherical pore diameters larger than $30 \,\mu m$ was trivial. Skewness of the pores is described in the sphericity histogram, which leads to the max ferret diameter being different than the equivalent spherical diameter. Generally, unavoidable keyholing pore formation is spherical and pushed away from the lasermatter interaction zone when the keyhole collapses toward the interior of the struts due to the recoil pressure generated from metal vaporization at the solidification front [82,83]. Secondary lack of fusion porosity (Fig. 5) yields non-spherical pores closer to the overhanging boundaries, between scan tracks and deposited layers, where material solidification can be challenging without the presence of sufficient input energy [84]. We report a minimal 0.01% presence of keyhole pores (Fig. 6) with roundness >50%, the majority of which have maximum ferret sizes of $<40 \,\mu\text{m}$.

Table 3 Selected exposure profile of the experimental specimens based on the manufacturing feasibility study for a 40 um layer recoating thickness

t = 40 um	Laser power (W)	Laser speed (mm/s)	VED or ED
Infill	320	1300	68.38 (J/mm ³)
Upskin	225	841	74.32 (J/mm ³)
Downskin	315	2700	36.46 (J/mm ³)
Std. contours	178	823	5.41 (J/mm ²)
On-part contours	180	638	7.05 (J/mm ²)
Edges	90	800	2.81 (J/mm ²)

Note: Further verification of the appropriateness of the selected profile is conducted through the part characterization (Fig. 3).

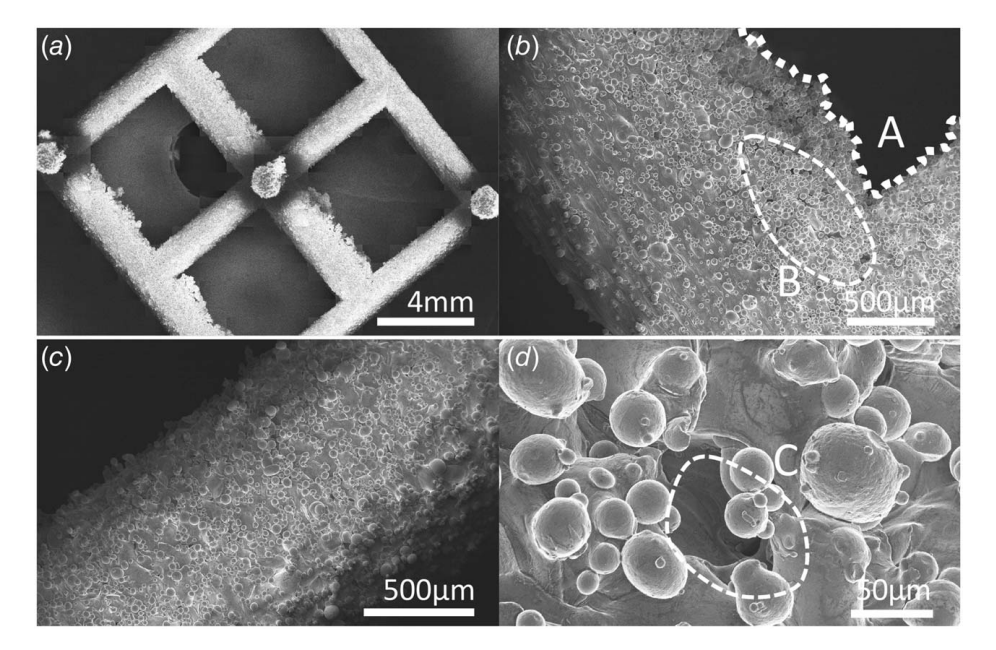


Fig. 5 As-built part imperfections from the SEM imaging of a unit cell manufactured with the default exposure profile [46]: (a) strut diameter variation and partially melt powder particles at the boundaries. Differences between struts manufactured with different angles are observable. The undersides of struts present increased surface roughness and unmelt powder particles, (b) strut curvature (waviness) (area A) and open pores (area B). A gradient of the surface roughness is apparent between the top surface and bottom surface of the struts, (c) partially melt pores attached to the molten substrate of a vertical strut. The surface roughness and strut curvature deviations are noticeably improved compared to the horizontally printed struts, and (d) open porosity (holes) at the surface layer accompanied by unmelt powder particles at the vicinity of the hole (area C). The sphericity and powder particle size can be observed.

The low magnification scan (using a voxel size of $54.09\mu\text{m}$) of all six architectures aimed at providing data about the effective as-built distributions of equivalent area circular strut diameters (Fig. 7). The print thickness of thin features is significantly affected by the steep overhang angles [47], with steeper angles (closer to the horizontal) being harder to bridge and a tendency to become oversized compared to close-to-vertical angles that approach better the CAD dimensions and can be somewhat undersized. Scans of all manufactured architectures revealed the absence of severe process-induced imperfections such as broken or bent struts, which can lead to severe diminishment of the macroscopic elastoplastic properties of the truss lattices [80].

Diameter measurements illustrate a clear variability of effective diameters compared to the target CAD diameter of 1 mm, which consequently can affect the relative density, and thus the elastic and failure properties of a finite-sized truss lattice. The deviation from the shape of a perfectly circular strut was leveraged through area measurement of multiple struts in a slice and the calculation of the averaged equivalent circle area diameter. A total of 300 equivalent strut diameter measurements were randomly sampled for each architecture, with three groups of struts (diagonal elements in both *X*–*Y* directions, Vertical elements in the *Z*-direction as shown in Fig. 3) consisting of an equal amount of 100 samples. For measuring the diameters from the scans, corrections according to the angle of measurement were performed to always measure the perpendicular to the long axis diameter of each strut.

The range of equivalent area circle diameter measurements for all lattices was within the range of 0.875-1.25 mm. A clear correlation between the highest angle (angle closest to the vertical direction Z in Fig. 4) and the smallest diameters can be observed. The accompanying correlation between the lowest angle and the largest diameters is seen to be due to the effect of overhangs increasing surface roughness through the presence of unmelt particles and curvature deviations (Fig. 5) resulting from the melt pool solidification process. A split can be observed in the histograms of the diagonal strut

populations attributed to the mixture of steeper, thus thicker, and intermediate angles, which print slightly thinner. The distribution of the intermediate features varies by the angles present in each geometry. The weighted means of the total measurements (N = 300) were calculated for all architectures based on the total number of struts in the strut group within the entire truss lattice of a certain architecture (weights) and the mean diameters of each equal-sized group. Overall, weighted means present a range of strut oversizing of 1–10%, in the truss lattice's interior depending on the rule of mixtures of different angles present in the architecture. The diameter distributions provide the boundaries for the expected peak stresses and elastic properties by affecting the effective relative density of the truss lattice rather than precisely predicting the expected mechanical properties due to potential manufacturing imperfections at the boundaries, different stress distributions in each architecture, and intricate geometric nonlinearities that appear during axial compression. Imperfections may arise from the manufacturing process formed by residual thermal stresses, challenges in the solidification of boundary edges, and imperfect cutting from the base plates, which can all affect the quality and mechanical characteristics of the boundary struts. Even though the WEDM cuts are renowned for their precision in terms of tolerances, cuts in three axes can still introduce the removal or addition (in the form of including part of the supporting structure) of excess material.

During the experimental and computational study of the finitesized truss lattice tests under axial compression in Secs.4.2 and 4.3, it is observed that the mechanical properties of the truss lattices exhibit low sensitivity to the imperfections mentioned above. For this particular configuration of exposure settings, build angles, and architectures, the mechanical behavior is sufficiently described by uniform strut diameters tuned to the characterization analysis and the experimental results. Strut under-sizing and over-sizing (local minima and maxima of the measurements) formed during the melt pool solidification process have little effect on the overall

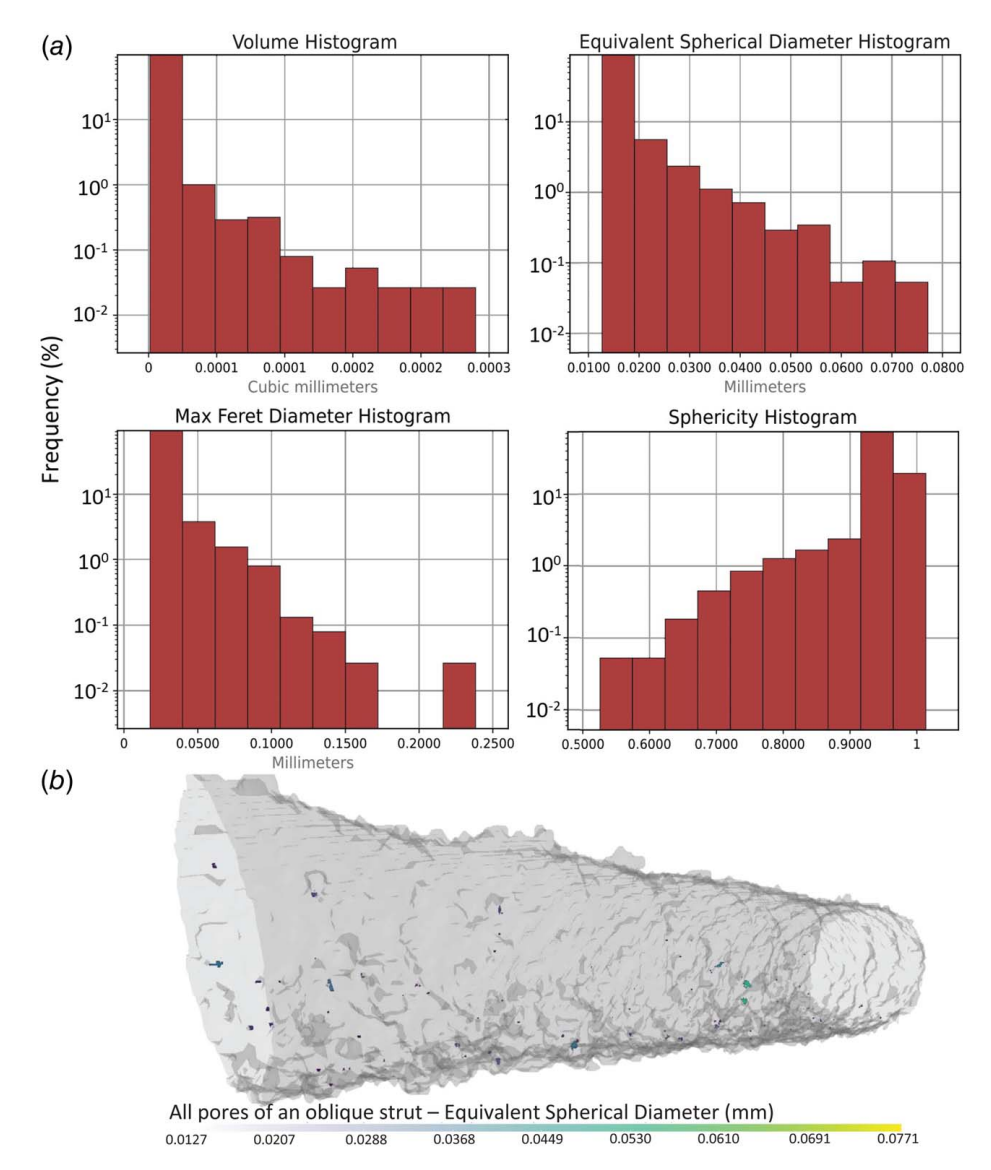


Fig. 6 (a) Total measured porosity of a unit cell is 0.01% using a voxel size of $10.2202\,\mu m$. Overall the amount and size of pores present is considered minimal and satisfactory. Distributions of porosity characteristics of struts manufactured with 48 deg and 73 deg inside a BT75 architecture's unit cell (log scale) are presented. The volume, equivalent spherical diameters, max ferret diameters, and dimensionless sphericity histograms for the 0.01% of pores are shown, with the pores being attributed to keyholing and (b) contour map of the equivalent spherical diameter of the pores in a 48 deg strut.

behavior. The imperfection sensitivity of the truss lattices is expected to change when reaching relative densities with strut sizes closer to the powder feedstock grain size. A quantification of the imperfection sensitivity in different relative densities exceeds the scope of this work but presents an open topic for further research.

4 Experimental Results

4.1 Material Testing. To characterize the tensile strength and stochastic features [45] of the 15-5 PH stainless steel powder that was used, with the selected exposure profile, a series of coupons (dogbones) were manufactured. Two different sizes of dogbones were manufactured with cross-sectional areas $W_1 = 2.5 \,\mathrm{mm}^2$ and $W_2 = 22.68 \,\mathrm{mm}^2$ to study size effects [44]. In particular, five sets of specimens with build angles of 0 deg, 30 deg, 45 deg, 60 deg, and 90 deg were manufactured to explore the influence of overhangs

in the mechanical properties of the specimens. These angles cover a broad range of angles that are in proximity to the angles that appear in the truss lattices (Fig. 7), with the exception of the 0 deg (horizontal) and 90 deg (vertical) specimens, which are commonly used in material specification sheets to characterize the bulk material properties. Both dogbone sizes were tested using an Instron 5969 frame (load-bearing capacity of 50 kN) with AVE2 video extensometer mounted for non-contact strain measurements and a Fujinon CF35HA-1 35 mm lens. The strain was measured via virtual extensometer dot tracking between the edges of the 7 mm and 23.81 mm gauges (Fig. 8), with marks approximately $4.5-6.5 \,\mathrm{mm}$ (W_1) and 20–23.5 mm (W_2) apart from each other. Automatic calibration of the strain gauge lengths was used, and the dot marks were ~1 mm each. The resolution of the optical strain measuring system was $0.5 \,\mu \text{m}$ with $\pm 0.5\%$ measurement accuracy (ASTM E83-16 Class B-1 compliant system with strain uncertainty no greater than ± 0.0001 mm/mm or $\pm 0.5\%$ of strain [85]). The specimens were tested as-built, without any further post-treatment or

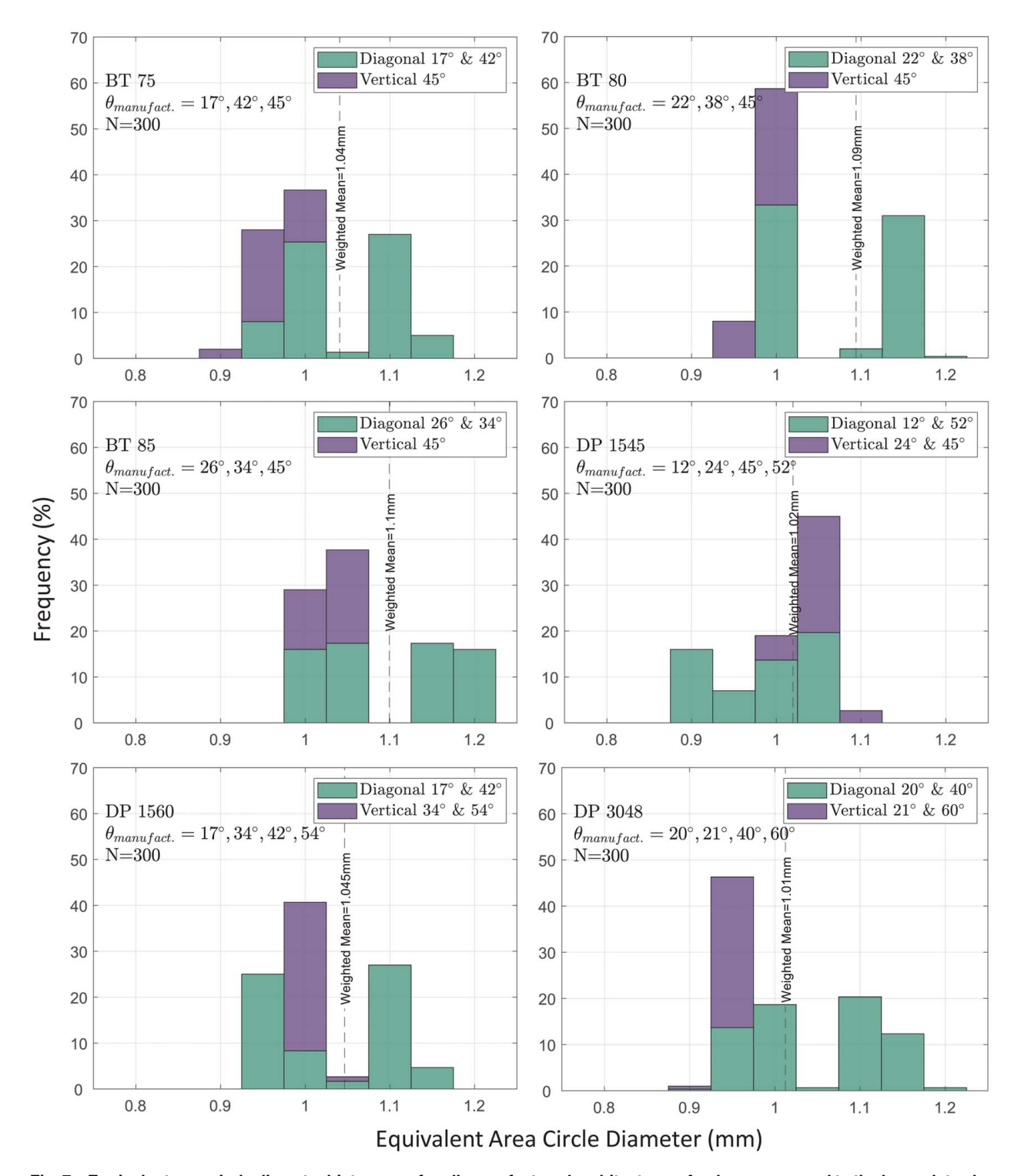


Fig. 7 Equivalent area circle diameter histograms for all manufactured architectures. Angles correspond to the base plate elevation angles (deviation from the horizontal XY plane in Fig. 4). Bin widths are set equal to the voxel size ($54.09\,\mu m$). Two groups of diagonal elements were measured (both directions), and all vertical elements were measured with 100 measurements per group, summing to 300 measurements per specimen. The maximum strut undersizing was 11.5%, and the maximum strut oversizing was 22.5%, with steeper (lower) angles facilitating larger oversizing. Strut undersizing appears in elements printed closer to the vertical direction Z.

polishing, to match conditions inside the truss lattices as closely as possible. The test method was a monotonic quasi-static strain-controlled tension with 0.01 strain/s applied until fracture.

Results of these tests are presented in Fig. 8. An analysis of the results was performed to extract information about the maximum elongation of the specimens, the ultimate tensile strength (UTS),

the elastic modulus, and the yield stress (Fig. 9). The thinner feature specimens present significantly higher standard deviations (Fig. 2 available in the Supplemental Materials on the ASME Digital Collection) for the max. elongations, UTS, and E, when compared to the larger specimens, which can be attributed to the effect of surface roughness on the cross-sectional area

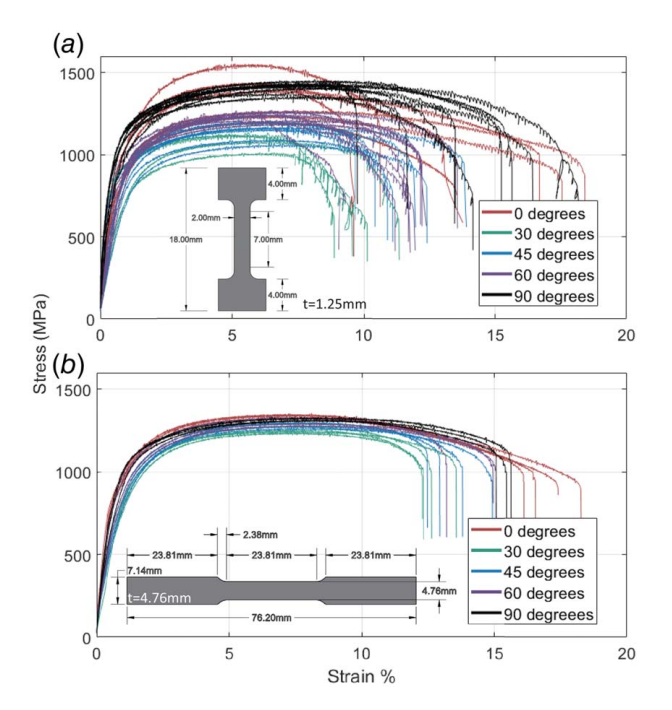


Fig. 8 Stress–strain curves from the monotonic tensile tests of two sizes of manufactured dogbone specimens (cross sections of (a) $W_1 = 2.5 \, \mathrm{mm^3}$ and (b) $W_2 = 22.68 \, \mathrm{mm^3}$, with various manufacturing elevation angles (inclinations in the Y-axis shown in Fig. 4) on the base plate. The dimensions of the dogbone specimens are presented in the figure. The thin-feature specimens present anisotropy apparent in their elastic properties, fracture strains, and UTS compared to the larger specimens manufactured with the same exposure profile shown in Fig. 3, due to a combination of effects such as the surface roughness, the number of grains in the gauge section, the porosity, and the microstructural texture.

measurement, number of grains in the gauge section, porosity, and microstructural texture [44]. Overall, these specimens are expected to represent more accurately the printed features inside truss lattices with low relative densities due to the similarities of their crosssectional areas (nominal areas of 2.5 mm² in the small dogbones versus 0.785 mm² in the truss lattice struts). The tensile properties of the bulk material are expected to be closer to the larger specimens for non-thin features. The larger specimens presented equal and higher UTS than the ones mentioned in the manufacturer's specification; elongations and yield stresses were within the manufacturer's range despite the change of the layer recoating thickness from $20 \,\mu \text{m}$ to $40 \,\mu \text{m}$. For all of the inclined elements, a clear pattern of diminished mechanical properties is seen to correlate with steep angle elevations for both small and large dogbone specimens. Estimates on the expected elastic modulus weren't available on the manufacturer's specification sheet; however, the literature has shown similar ranges of variability for vertically printed 316L [44]. Further investigation of the microstructure near the boundaries of inclined struts with thin features is necessary to understand the melt pool solidification mechanisms that lead to this behavior, but that study is beyond the scope of this work.

4.2 Mechanical Behavior of the Bowtie Family of Architectures. The manufactured truss lattice architectures were monotonically tested in axial compression to determine their elastic properties, peak stresses, strains at the peak stresses, deformation modes, and energy absorption capabilities. For the mechanical testing of the geometries, the same Instron 5969 frame (load-bearing capacity of 50 kN) with AVE2 was used as in Sec. 4.1, with the specimens resting unconstrained on steel compression platens. The digital image correlation (DIC) capabilities

of AVE2 were utilized to capture lateral strain and calculate the Poisson's ratio of the lattices, this time using a Fujinon HF9HA 9 mm lens with measurement resolution of $1.5 \mu m$ and accuracy of ±1% (ASTM E83-16 Class C compliant system with strain uncertainty no greater than ± 0.001 mm/mm or $\pm 1\%$ of strain [85]). A speckle pattern was painted on the front face of the geometries, while every other strut was painted black to increase contrast and reduce the visibility of interior strut planes in the DIC measurements. The Poisson's ratio was consistently measured by virtual strain gauges placed in the DIC software at the center of each side and top/bottom boundary. Three measurements were taken and averaged to determine the axial and lateral strain at 0.01 axial strain (in both the correlated experimental results and computational simulations) to ensure contact of the top and bottom end struts with the compression plates. A displacement-controlled method was used with a quasi-static rate of 1 mm/min up to 25 mm of displacement (approx. 40% strain). The Poisson's ratio, axial modulus, and total energy absorption (Eq. (2)), where P is the applied force, d is the applied displacement, and m is the mass of the specimen) of the architectures were calculated and compared between all architectures based on the experimental force-displacement (Supplementary Figs. 3 and 4 available in the Supplemental Materials on the ASME Digital Collection) and stress-strain curves (Figs. 10 and 11). The presence of manufacturing imperfections, such as missing struts, is known to affect the compressive properties of the truss lattices considerably [80]. This experimental study focuses on reporting findings without the presence of any major manufacturing imperfections.

$$TEA = \int_{0}^{d} P(x) dx$$
 (2)

In Figs. 10 and 11, points A (x's) indicate the end of the elastic branch, and points B (stars) indicate the peak stresses. For the case of the bowtie architectures, a relatively small purely elastic area exists up to point A, and beyond that, a non-linear curve is observed until the plateau before the first peak drop. Excellent agreement between the stress-strain curves and deformation modes of both specimen repetitions was observed, even in large plastic strains. During the experiment, small displacements were observed up to the end of the elastic region (point A). At approximately 5% of strain, rotation of the top and bottom end struts starts becoming noticeable. At strains larger than 10% and up to the first load drop, significant deformation inside the truss lattice becomes noticeable to the observer with remarkable deformations of interior unit cells, observable curvature across the height of the specimen, and out-of-plane movement of the body of the truss lattice. After the first load drop, we observe a layer-by-layer collapse and the formation of horizontal bands of individual buckled layers due to the incremental yielding of planes of unit cells, which is depicted in the stress-strain curves with numerous hills and valleys. Large out-of-plane deformations of the truss lattice accompany this behavior. Further peaks and valleys are achieved by the densification of the collapsed layer and the creation of a new failure plane following the same mechanism. In the post-peak regime, even though the geometry has reached a state of progressive collapse, the hills, and valleys of layer-wise densification come very close to the first peak load, allowing for significant energy dissipation, which presents itself as additional area under the force-displacement curves. While fracture is observed at the regions of high bending stress on the diagonal beams, the struts remain largely connected at the nodes. The architectures reach their peak stresses at very large strains (>10%), thus demonstrating distinct geometric non-linearities by constant reduction of their characteristic angles. The bowtie $\theta = 80 \deg$ geometry exhibits the most ductile plateau drop, followed by the bowtie $\theta = 85 \deg$ architecture, and bowtie $\theta = 75 \deg$ comes third by marginal differences. The $\theta = 85 \deg$ bowtie attains the highest peak stresses out of the three architectures with equal $\rho_{UC}^* = 5\%$, with the $\theta = 80$ deg being next and the $\theta =$

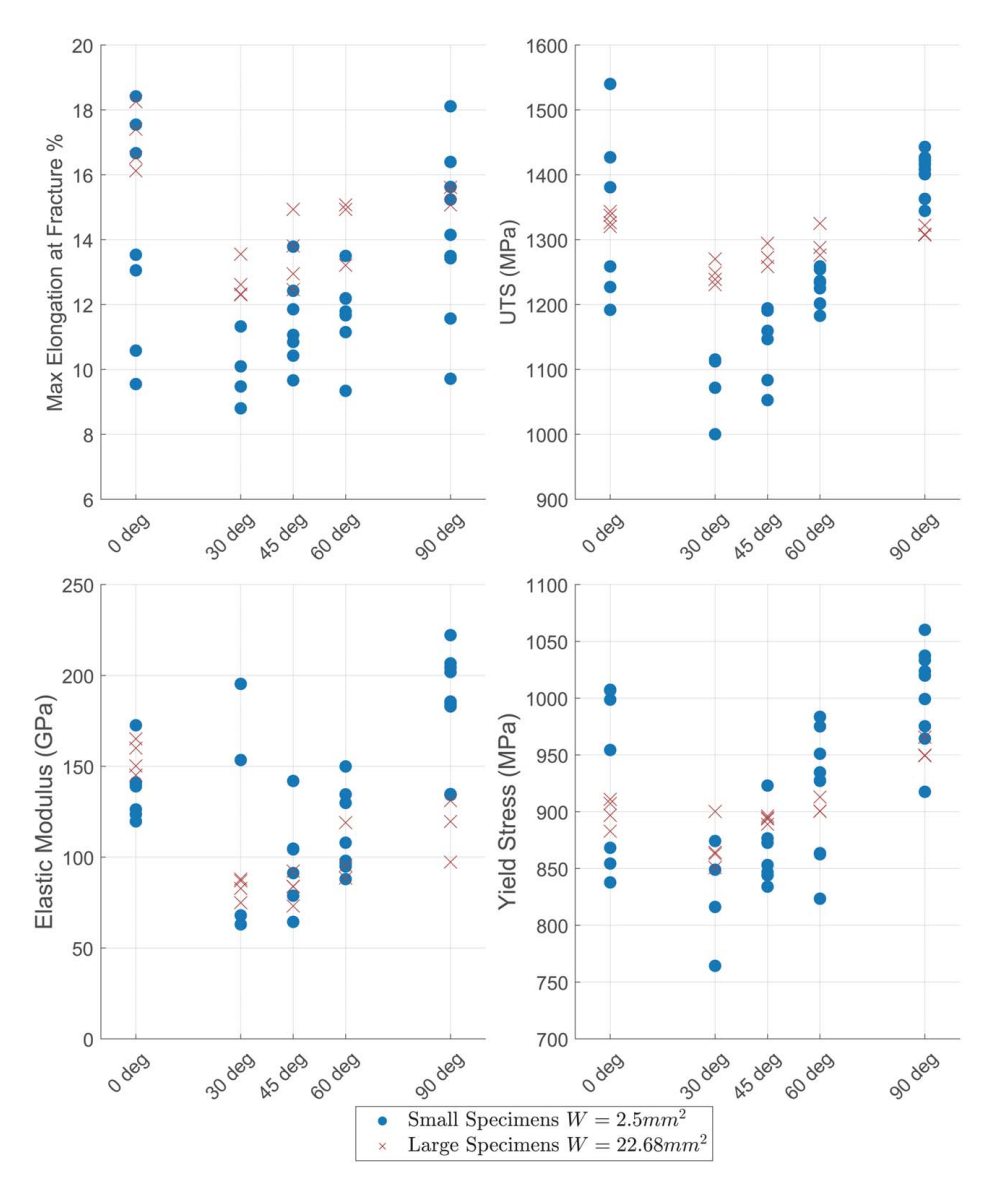


Fig. 9 Analysis of the stress–strain curves of both small and large $40\,\mu m$ layer dogbone populations ($W_1=2.5\,mm^3-$ circles and $W_2=22.68\,mm^3-$ x's). Good agreement with the $20\,\mu m$ material specification is observed for most of the maximum elongations, while the UTS and yield stress values present greater variance, especially for the smaller specimens. The elastic moduli measurements present a wide range of values. The larger specimens illustrate substantial consistency between measurements of their as-built properties compared to the smaller specimens. Altogether, inclined elements present inferior mechanical properties compared to their vertical and horizontal counterparts.

75 deg being last. This correlates directly with these architectures' axial and transverse moduli following the same exact pattern (Fig. 2). Reversely, the lower the axial and transverse stiffness is for the family of bowtie architectures, the more auxetic they are, with Poisson's ratio being negatively correlated to the stiffness of the architecture.

4.3 Mechanical Behavior of the Double Pyramid Family of Architectures. The same experimental configuration and testing method were used for testing the auxetic double pyramid architectures. The double pyramid architecture exhibits significantly higher stiffness and peak stresses compared to the bowties. The significant differences in the axial stiffness of the double pyramids are also noticeable in Fig. 11. In the $\theta_1 = 15$ deg; and $\theta_2 = 45$ deg and $\theta_1 = 15$ deg and $\theta_2 = 60$ deg architectures, plastic deformation is apparent between points A and B and before 5% strain, with excessive rotation

of the nodes in the middle of the height of the architecture. Rotation and deformation of these nodes ensue, up to the peak, until fracture of the diagonal elements takes place in the vicinity of their nodes, accompanied by buckling of the longer inclined elements. As in the case of the bowties, the formation of a collapse zone closely coincides with the peak stress. The post-peak region for the two aforementioned architectures is characterized by increasing deformation and buckling of the struts located in the center of the geometry and a major drop in the attainable peak stresses due to the large aspect ratio of their unit cells, not allowing the densification of the unfractured zones of unit cells around the collapsed zone. Horizontal failure bands form close to the center of the specimen, where the fractures predominately occur, with the 15–45 developing an inclined failure plane in strains >15%.

The $\theta_1 = 30$ deg and $\theta_2 = 48$ deg double pyramid geometry illustrates a slightly different failure mode compared to the other two double pyramids due to the different aspect ratio and geometrical

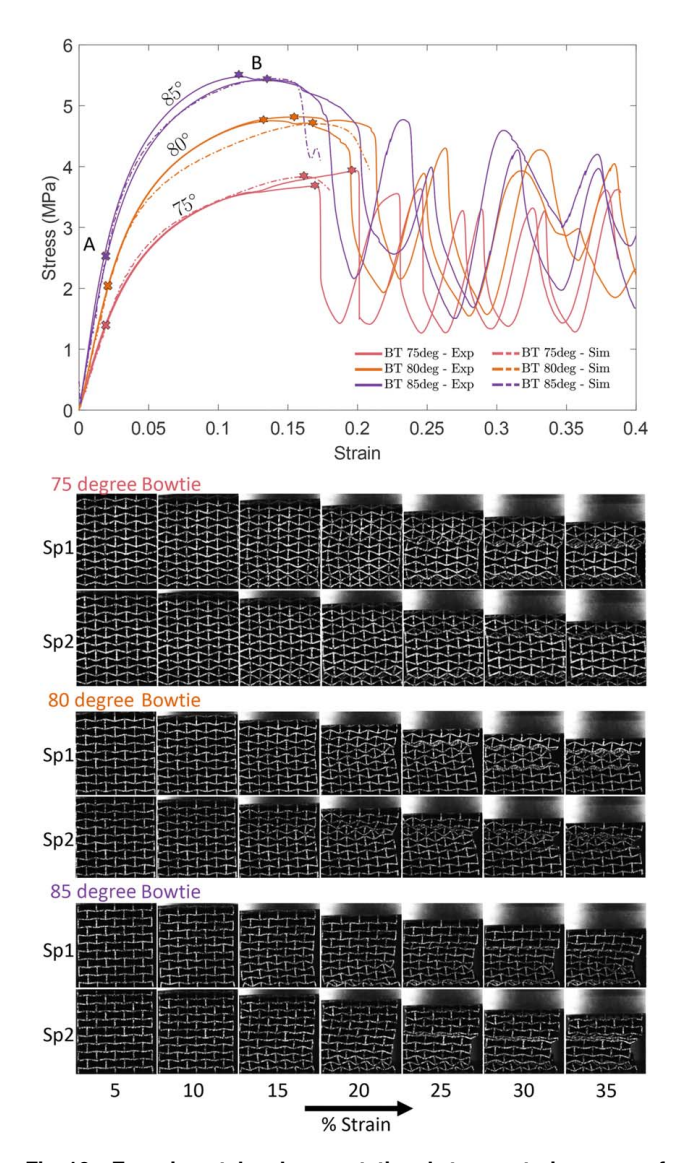


Fig. 10 Experimental and computational stress–strain curves of the auxetic bowtie architectures under monotonic axial compression, with the deformation modes presented during strain progression. Two experiments were conducted per architecture, marked with Sp1 and Sp2, respectively. Points A indicate the end of the elastic branch, and points B indicate the peak stress values. Hills and valleys correspond to the plane-by-plane progressive collapse of bands of unit cells.

features of its unit cells. In this architecture, deformations start becoming apparent after 5% of strain. Interestingly, the 30-48 exhibits a second linear branch after point A and past the yield of its diagonal elements, up to reaching its peak stress at point B. In the plastic regime, fracture of the struts takes place in a horizontal band around the center of the specimen. Its post-peak response is characterized by significant densification, similar to the bowties, due to the high number of horizontal fracture zones available to densify and progressively collapse. The higher number of shorter struts leads to higher redundancy for stress redistribution through self-contact with less displacement when a horizontal collapse band forms. Despite the fact that the 30-48 architecture contains more and less slender struts, its stiffness is significantly lower than the other double pyramids, owing to its geometrical features, as predicted from the explorative unit cell calculations (Fig. 2). Overall, double pyramids exhibit higher total energy absorption, primarily in the case of $\theta_1 = 30 \deg$ and $\theta_2 = 48 \deg$ and to a lesser effect in the case of the other two architectures. All of the

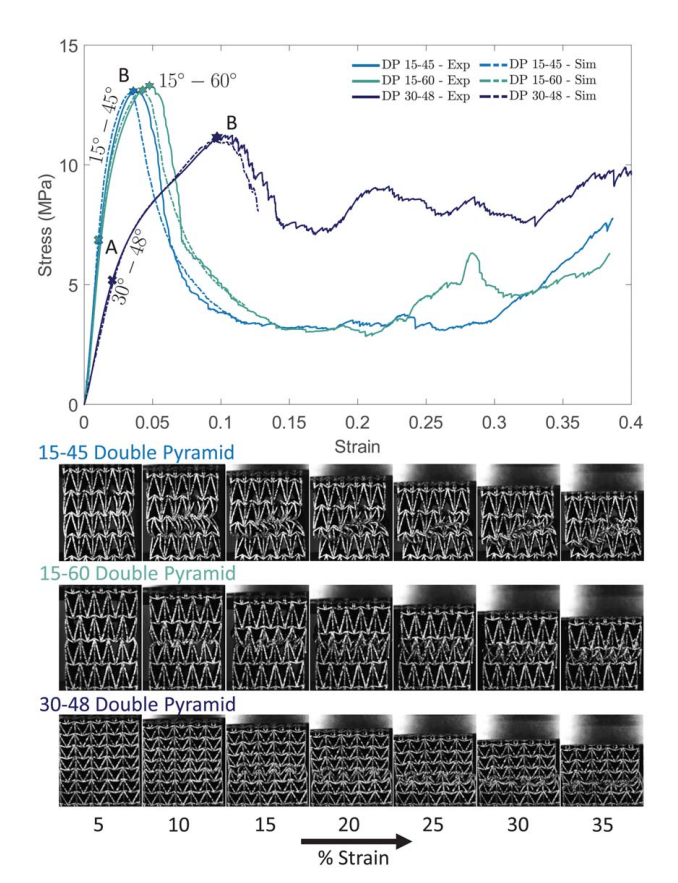


Fig. 11 Experimental and computational stress–strain curves of the double pyramid architectures under monotonic axial compression, with the deformation modes presented during strain progression. One experiment was conducted per architecture. Points A indicate the end of the elastic branch, and points B indicate the peak stress values.

double pyramid geometries exhibited a fracture-dominated failure, with strut fracture happening at the diagonal elements near the nodes in the vicinity of the peak load, where the higher stress concentrations are located. In both bowtie and double pyramid geometries, the effects of friction and surface roughness can affect the self-contact behavior when the geometries collapse and densify in the post-peak region. While the double pyramid 15–45 and 15–60 architectures exhibit increased axial stiffnesses and peak loads due to their favorable geometrical features, it is observed that a near cubic unit cell design such as the 30–48 could significantly increase the area under the force–displacement curves.

Measurement of the change of the characteristic angle θ , in each one of the architectures revealed patterns between the same family of architectures and the same angle family for the two characteristic angle double pyramids (Fig. 12). Specifically, all bowties present the same angle reduction up to the end of the elastic branch (point A) and extend up to large strains ($\sim 8\%$ of strain). The 75 deg bowtie presents a plateau region where the angle remains almost the same before the peak, which can be attributed to strain localization in locations other than the ones measured due to plasticity. All of the bowties experience deviations within repetitions of the same architecture in the measured characteristic angles once they enter the plastic regime due to the high nonlinear deformations taking place. The double pyramid architectures present consistent angle changes within the different architectures, with all θ_1 angles exhibiting minor reductions with strain propagation and all θ_2 angles experiencing significant changes. This agrees well with the fact that in the shorter diagonal elements the stresses concentrate in the finite element analysis and are the first elements to fracture in the experiments. The significant

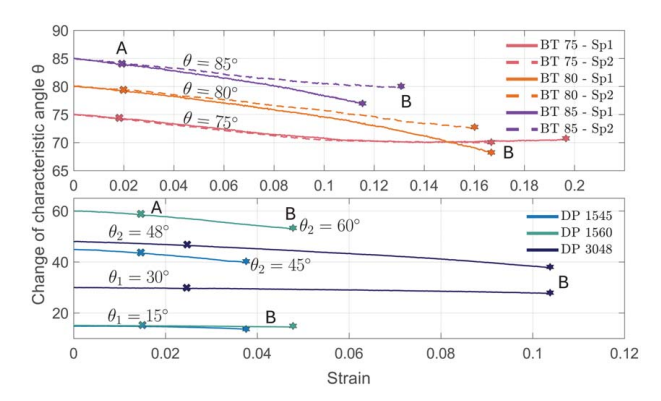


Fig. 12 Experimentally measured angle change plotted against strain up to the peak stress point B for each one of the six architectures. The angle deviations were measured at the center of each truss lattice. The bowties follow similar decreases in $\Delta\theta$, even past the end of the elastic branch A. The angle change in the 75 deg bowtie geometry experiences a plateau around 70 deg, while the 80 deg and 85 deg bowties exhibit larger angle reductions. The double pyramids experience similar patterns of angle reduction for each one of their characteristic angles. Notably, angles θ_1 experience minor angle changes while angles θ_2 experience dramatic reduction with strain progression.

geometrical non-linearities involved in the deformation of the architectures translate to changes in their elastic properties throughout strain propagation.

5 Computational Verification of Experiments and Parametric Finite Element Analysis

A finite element validation of the experimental results was performed using ABAQUS CAE/EXPLICIT (Dassault Systémes, Johnston, RI) [73], using a minimum of approx. 3,000,000 C3D4 solid continuum tetrahedral elements per architecture. To simplify the anisotropy inherently present in the truss lattice struts and reduce the computational burden of having multi-material truss lattices, the models were calibrated to the experiment inside the range of measured bulk and truss material properties. Specifically, for the BT architectures, $E = 140 \, \text{GPa}$ was used, and for the DP architectures,

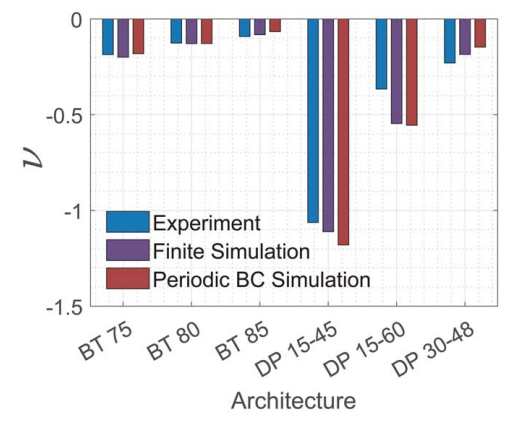


Fig. 13 Poisson's ratio of architectures from experiments (averaged), finite-sized and periodic boundary condition computations (Fig. 1). The Poisson's ratios were calculated at 0.01 axial strain using the procedure described in Sec. 4.2 for the finite-sized simulations and experiments, while they were calculated at infinitesimal strains at the boundaries of the unit cell in the explorative periodic boundary condition simulations. The double pyramid geometries exhibit remarkably lower Poisson ratios compared to the bowtie geometries.

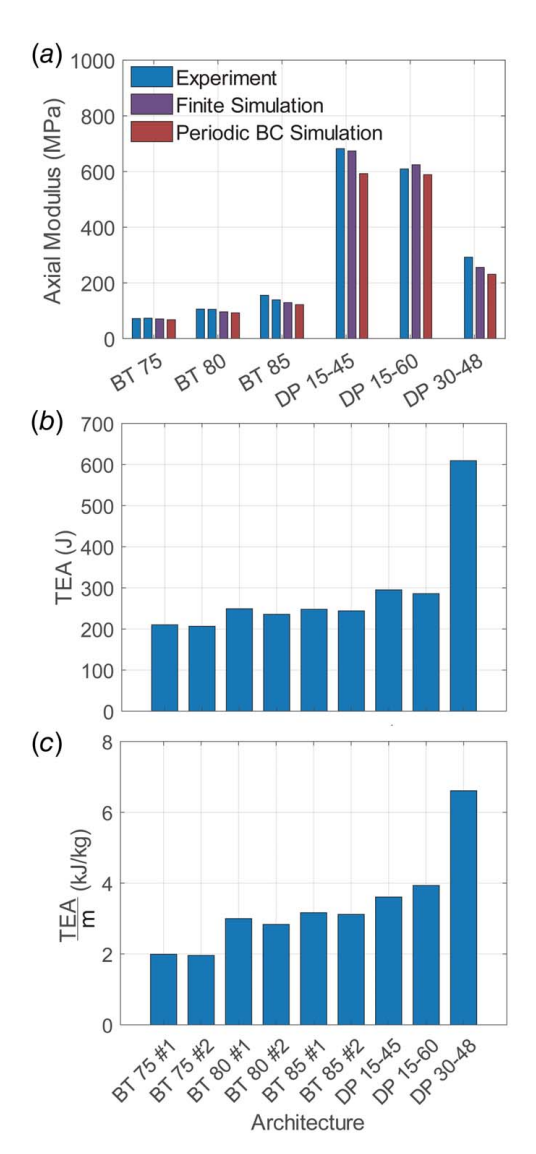


Fig. 14 (a) Axial modulus of the experimental specimens and computed modulus from their respective finite-sized and periodic boundary condition truss lattice simulations. The architectures follow the findings of the finite element computations, (b) total energy absorption of the experimental specimens at 25 mm of displacements (Eq. (2)). The 30–48 double pyramid presents the highest total energy absorption owing to its high achieved peak stresses and its unit cell aspect ratio, (c) total energy absorption over the mass of each specimen at 25 mm of displacement. A slight change in the total energy absorption pattern is observed when leveraging the mass of the specimens in the calculation of the normalized over the mass total energy absorption.

E=75 GPa was used due to the additional presence of lower stiffness steep angles (<45 deg) in long vertical struts during manufacturing. The Poisson's ratio used was $\nu=0.30$. The plasticity flow law was defined as 850 MPa at 0.0 strain, 1050 MPa at the range of 0.075–0.185 strain, and 100 MPa at 0.2 strain. The compressive plates were modeled as frictional analytical rigid surfaces with a friction coefficient of $\mu=0.6$ due to the increased surface roughness of as-built parts (in the range of $\sim 30\,\mu\text{m}$) [86,87], and surface contacts were tracked at the boundaries. Secondary nodes of diagonal elements in the vicinity of the top/bottom boundaries, which can also touch the compressive plates at large strains, were also tracked as surface contacts. The applied displacement was 11.5 mm for the bowtie architectures and 7.5 mm for the double pyramid architectures for a total duration of 1100 s and 720 s,

respectively (quasi-static displacement rate of 0.625 mm/min), to study the compressive behavior up to the first load drop. A further prediction of the densification beyond this would require general contact tracking, which significantly increases the computational time and is considered beyond the scope of this work.

Appropriate mass scaling was used to increase the stable time increment to a minimum of 0.001-0.0025 s to maintain a balance between accuracy and computational efficiency. To computationally model the experimentally tested architectures, an equivalent uniform diameter was tuned to match the experiment in the range of the CT scan observed diameters. Specifically, the values that were used were 0.98 mm for BT75, 1.015 mm for BT80, 1.01 mm for BT85, 1.075 mm for DP1545, 1.045 mm for DP1560, and 1.06 mm for DP3048. Overall, effective diameters were in the range of $1.03 \text{ mm} \pm 0.05 \text{ mm}$ for all printed architectures. The models were subsequently less sensitive to changes in E, YS, and UTS within the given experiment ranges. Strut oversizing and undersizing during the melt pool solidification process (Fig. 7), and the unintentional addition/removal of material at the boundaries during WEDM cuts of the supports can explain the deviations from the elastic properties of an equivalent 1 mm truss lattice.

First, the computational verification of the experiment was conducted. The agreement between the computational models and experiments has been satisfactory for the axial moduli, peak stresses, and observed Poisson ratios (Figs. 10, 11, 13, and 14). Small deviations of the experimentally measured Poisson's ratio from the simulations of the double pyramids were attributed to the fact that the two-dimensional DIC measurements were taken at the edge nodes of the two-dimensional cuboid rather than the center of the three-dimensional structure (Fig. 13). The lateral strains there were observed to fluctuate a little due to strain localizations. The computational models agree well with the existing literature [6], where the critical struts for the Von-Mises stress, logarithmic strain, and plastic strain concentration are always the diagonal ones, with them dominating the non-linear and fracture behavior of the architectures. Consequently, manufacturing deviations discussed previously can remarkably affect the overall mechanical behavior when they appear to concentrate in those

Additionally to the computational verification of the experiments, parametric models were developed based on the experimentally calibrated model to describe the behavior of the architectures at different relative densities of 2.5%, 10%, 15%, and 20% (Fig. 15). These

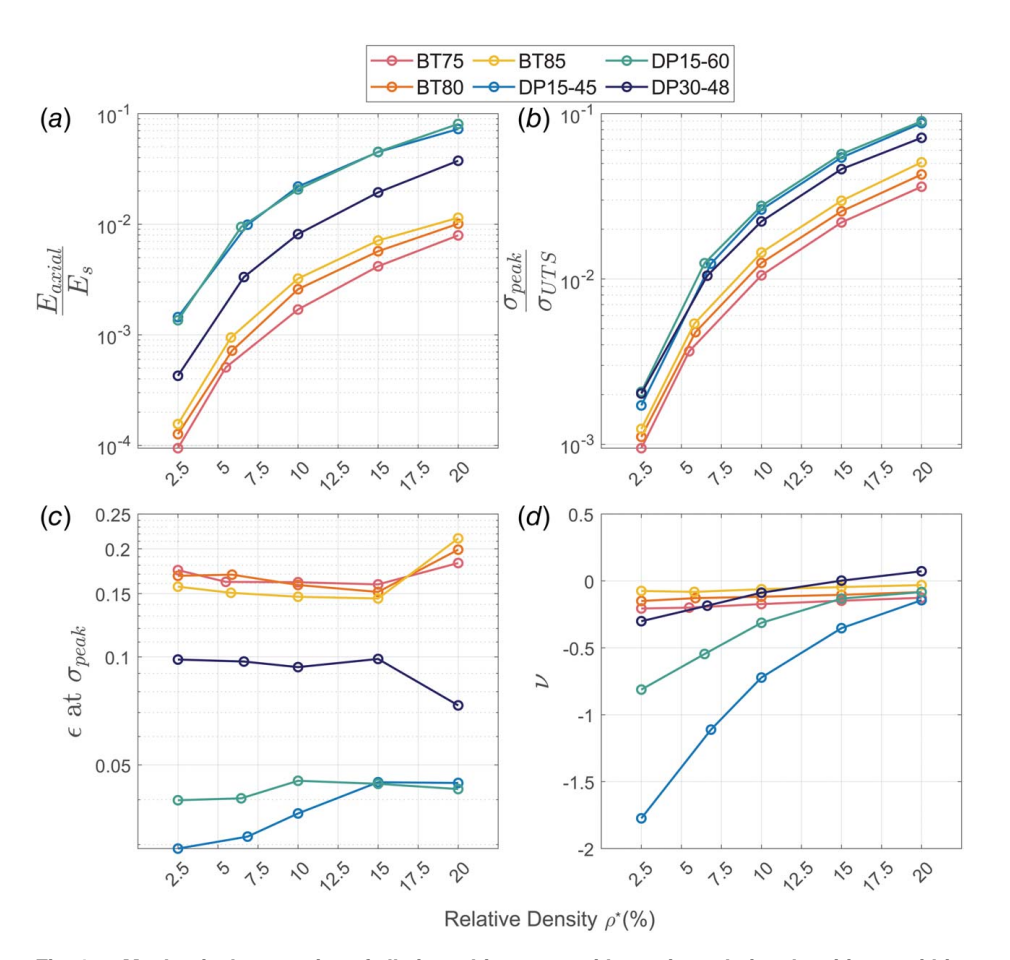


Fig. 15 Mechanical properties of all six architectures with varying relative densities ρ , within the range of 2.5–20%: (a) normalized axial modulus over the modulus of the bulk solid ($E_s=140$ GPa for the bowties and $E_s=75$ GPa for the double pyramids), (b) normalized peak stresses over the bulk material's ultimate stress ($\sigma_{\rm UTS}=1050$ MPa for all computations), (c) strain at the location of the peak stress, and (d) Poisson's ratio measured at 0.01 strain. The sensitivity to changes in the relative density is observed to be close to the expected quadratic scaling for the achieved stiffness, while for peak stresses, the scaling coefficient appears to be slightly smaller, close to the expected power of 1.5 for bending-dominated architectures (Table 4). Strains at the peak don't appear as sensitive to significant alterations of ρ . The Poisson's ratio ν increases together with the increase of relative density, and in the case of the 30–48 double pyramid architecture, it becomes >0 for ρ > 15%. This increase could be attributed to the nodal stiffnesses playing a more dominant role at higher relative densities.

Table 4 Scaling law coefficients (Eq. (4)), derived from the parametric finite-sized computations for each one of the six experimentally tested architectures

	Stiffness		Strength	
Architecture	C	n	С	n
BT 75	0.2364	2.116	0.6185	1.764
BT 80	0.3046	2.11	0.7538	1.782
BT 85	0.2031	1.784	0.9536	1.824
DP 1545	1.235	1.757	1.48	1.753
DP 1560	1.89	1.962	1.387	1.696
DP 3048	1.347	2.227	1.052	1.666

Note: The architectures exhibit exponent *n* values closer to two, indicating a mostly bending-dominated behavior.

relative densities were based on a finite-sized lattice definition due to the need to include plate contacts and study non-periodic deformations related to the failure response. The desired relative densities were achieved with an adjustment of the uniform strut diameter. Relative densities of <10% were explored with civil infrastructure applications in mind [6], and >10% pertain to high-energy absorbing material applications and biomaterials [11,46,88]. Changes in the strut diameters in a wide range of values can generate variable contact conditions at the top and bottom boundaries. During the parametric design of the finite-sized truss lattice architectures, the secondary contact distance of the top and bottom nodes connecting the diagonal elements was kept constant by adjusting the length of the vertical end struts, keeping the contact distance of the experimental truss lattices as the reference. Hence, the vertical strut length becomes equal to L_{leg} .

$$L_{leg} = L_0 + (R - R_0) (3)$$

where L_{leg} is the adjusted vertical top and bottom strut length, L_0 is the length of top and bottom struts of the experimentally tested truss lattices, R is the radius of the struts for the desired relative density, and R_0 is the effective uniform radius of the struts for the case of the experimentally tested truss lattices. This adjustment took place to maintain consistency between the same architectures with different relative densities and avoid alteration of the contact behavior at the boundaries, which can consequently suppress auxetic deformation in the top and bottom unit cells.

The computational results of steel auxetic truss lattices with different relative densities ρ illustrate non-linear scaling of the mechanical properties for the cases of the normalized moduli and normalized peak stresses (Fig. 15). In particular, the measured axial stiffness and peak stresses follow distinct patterns for all architectures. The architectures that exhibit higher axial stiffnesses also exhibit higher peak stresses. The 15–60 double pyramid presents the highest peak stresses, marginally followed by the 15-45, and third is the 30-48 double pyramid architecture. A significant difference is observed in the axial stiffnesses and peak stresses of the bowtie architectures, out of which the 85-degree specimen achieves the highest stiffness and peak stresses, followed by the 80 and 75-degree specimens. The strain at the peak of the architectures doesn't appear to be as sensitive to changes in relative density. However, the bowtie architectures follow the same pattern of variation for strain at the peak, with the double pyramids presenting significant variations from each other and for different relative densities. The 30-48 double pyramid is significantly more ductile, with strains at the peak in the range of 0.072-0.095, while the 15-45 and 15-60 architectures exhibit strains at a peak in the range of 0.029-0.046. This is expected due to the notable differences in axial moduli of the architectures; however, small local variations owing to the geometry and geometric non-linearities exist. The observed auxeticity for low relative density double pyramids (<15%) is remarkably higher than in the case of the bowties but tends to diminish at relative densities >10%. Overall, all

architectures tend to have diminishing Poisson's ratios with an increase in their relative densities. For the double pyramids, this reduction appears to be more dramatic. A transition from auxetic to non-auxetic is observed at relative densities >15% only in the case of the 30–48 double pyramid, which is also accompanied by a drop of its ductility at the ultimate stress point. This can be explained by the nodal stiffness increasing at higher relative densities.

From the findings of the parametric finite-sized computations for each one of the six architectures, the scaling law coefficients were calculated (Table 4 and Eq. (4)). The scaling laws [12] present a prediction of how the material properties scale with changes in the relative density of the material for relative densities <50%. For stiffness, exponent values ~1 indicate stretching-dominated materials, while values ~2 indicate a bending-dominated response. Similarly, for strength, the exponent value that indicates a stretching-dominated behavior is ~ 1 , and the exponent in the case of a bending-dominated response is ~1.5. $\phi_{lattice}$ corresponds to the lattice material property and ϕ_{solid} corresponds to the bulk solid material property. The coefficients were calculated from Fig. 15, for the axial stiffness and peak strength. Scaling coefficients consistent with bending-dominated deformation were found as expected, with nuanced deviations from each other due to the geometrical variations in the unit cells of the architectures.

$$\phi_{lattice} = \phi_{solid} \cdot C \cdot (\rho^*)^n \tag{4}$$

6 Conclusions

We report findings on the laser powder bed fusion additive manufacturing and axial compressive behavior of steel auxetic (negative Poisson's ratio) truss lattice materials. Two families of auxetic materials with re-entrant angles were studied; an auxetic bowtie geometry and an auxetic double pyramid geometry. After conducting an explorative round of finite element analysis for unit cells with periodic boundary conditions from both families, six unit cells with varying characteristic geometrical features were designed based on covering a range of Poisson's ratios and transverse moduli. The transverse modulus was selected because of its direct correlation with the Poisson's ratio and lateral compliance of the truss lattices. The architectures studied were the $\theta = 75 \deg$, $\theta = 80 \deg$, and $\theta =$ 85 deg for the bowtie family of architectures. For the two-angle family of double pyramids the angle combinations of $\theta_1 = 15 \deg$ and $\theta_2 = 45 \deg$, $\theta_1 = 15 \deg$ and $\theta_2 = 60 \deg$, and $\theta_1 = 30 \deg$ and $\theta_2 = 48 \deg$ were studied. Manufacturing of truss lattices with constant target relative densities of $\rho = 5\%$ took place using precipitation hardening stainless steel 15-5 and a custom exposure configuration derived from an exposure parameter study. The solidified parts were checked for their print quality, and their manufacturing deviations were quantified using scanning electron microscopy and X-ray computed tomography. Tensile testing samples (dogbones) were manufactured to explore the influence of overhang angles on the mechanical properties of thin and thick print features. Mechanical testing of the architectures under axial compression was performed to determine the elastic properties, peak stresses, deformation modes, energy dissipation features, and Poisson's ratios of the manufactured architectures. Finite element computations were performed to validate the experimental results, and a parametric analysis was performed based on these simulations to predict the change in mechanical properties of architectures at various relative densities. Overall, we report a comprehensive study from design to mechanical testing of auxetic steel architected truss lattice materials, the key findings of which are summarized as follows:

(1) Architectures from different unit cell families with the same design relative densities of $\rho = 5\%$, exhibit significantly different elastic properties, peak stresses, peak strains, failure modes, Poisson ratios, and energy absorption capabilities, owing to their unique geometrical features. This presents a unique opportunity to design tailor-made architectures to

- precisely meet specific engineering demands towards a performance-based design of metamaterials. Similarities in the crushing modes of specimens from the same family of unit cells exist.
- (2) The presence of undersized and oversized struts affects the effective diameters of individual struts significantly and thus the as-built mechanical properties of the architectures (Fig. 15). A low sensitivity to melt pool solidification-induced imperfections was observed, which allowed the tuning of computational models to the experiments using uniform strut thicknesses close to the weighted mean of the equivalent area circle diameters. Further study of the correlation of the alloy microstructure to the imperfections present in the lattices, as well as research on the imperfection sensitivity for strut thicknesses close to the grain size of the powder, is necessary.
- (3) Overhung struts increase the variance of mechanical properties for thin print features, specifically influencing the Young's modulus, UTS, elongation at fracture and to a lesser degree the yield stresses of said struts.
- (4) Consistent reproducibility was noted in the truss lattice structures manufactured through LPBF across similar architectures. This can be considered a side effect of the low imperfection sensitivity.
- (5) The evolution of the characteristic angles of the architectures was experimentally measured, revealing similarities between architectures of the same family, particularly in the elastic region, and similarities within the same characteristic angle for the two-angle double pyramid family of architectures. The change of characteristic angles $\Delta\theta$ leads to geometric non-linearities, which affect the elastic properties of the truss lattices with strain progression.
- (6) Even though computational models exhibit remarkable sensitivity to the input parameters, it was demonstrated that they can provide a satisfactory qualitative and quantitative prediction of the actual experimental behavior when properly tuned to each architecture by leveraging the manufacturing uncertainties of the various mixtures of overhang angles present in truss lattices as a bulk, instead of explicitly modeling anisotropy in truss lattices.
- (7) Changes in the mechanical properties of auxetic truss lattices with changing relative densities present significant nonlinearities, following the scaling relations as expected. Changes in the material properties in the range of their observed std. deviations were observed to affect the compressive behavior to a much lesser extent.

Acknowledgment

S. Gerasimidis would like to acknowledge the financial support of the National Science Foundation (NSF CAREER Grant No. 2044705). The authors would also like to thank Dr. Richard Church and Professor John Hart from MIT for their valuable assistance with the CT imaging, Mr. Dave Follette for his help with manufacturing the truss lattice specimens, and Mr. Mark Gauthier for his significant guidance with lab work.

Conflict of Interest

Researchers report no conflict of interest due to financial or personal relationships that could influence the findings of this work.

Data Availability Statement

The datasets generated and supporting the findings of this article are obtainable from the corresponding author upon reasonable request.

References

- Rastegarzadeh, S., Huang, J., and Wang, J., 2023, "Architected Cellular Materials for Aerospace Components Design and Manufacturing," p. V001T01A007.
- [2] Liu, Q., 2006, "Literature Review: Materials With Negative Poisson's Ratios and Potential Applications to Aerospace and Defence," p. 47.
- [3] Bohara, R. P., Linforth, S., Nguyen, T., Ghazlan, A., and Ngo, T., 2023, "Anti-Blast and -Impact Performances of Auxetic Structures: A Review of Structures, Materials, Methods, and Fabrications," Eng. Struct., 276.
- [4] Cui, H., Yao, D., Hensleigh, R., Lu, H., Calderon, A., Xu, Z., Davaria, S., Wang, Z., Mercier, P., Tarazaga, P., and Zheng, X. R., 2022, "Design and Printing of Proprioceptive Three-Dimensional Architected Robotic Metamaterials," Science, 376(6599), pp. 1287–1293.
- [5] Hedayati, R., Güven, A., and van der Zwaag, S., 2021, "3D Gradient Auxetic Soft Mechanical Metamaterials Fabricated by Additive Manufacturing," Appl. Phys. Lett., 118(141904).
- [6] Tzortzinis, G., Gross, A., and Gerasimidis, S., 2022, "Auxetic Boosting of Confinement in Mortar by 3D Reentrant Truss Lattices for Next Generation Steel Reinforced Concrete Members," Extr. Mech. Lett., 52.
- [7] Salazar, B., Aghdasi, P., Williams, I. D., Ostertag, C. P., and Taylor, H. K., 2020, "Polymer Lattice-Reinforcement for Enhancing Ductility of Concrete," Mater. Des. 196
- [8] Xu, Y., Zhang, H., Gan, Y., and Šavija, B., 2021, "Cementitious Composites Reinforced With 3D Printed Functionally Graded Polymeric Lattice Structures: Experiments and Modelling," Addit. Manuf., 39.
- [9] Zhou, G., Ma, Z.-D., Li, G., Cheng, A., Duan, L., and Zhao, W., 2016, "Design Optimization of a Novel NPR Crash Box Based on Multi-objective Genetic Algorithm," Struct. Multidiscipl. Optim., 54(3), pp. 673–684.
- [10] Babaee, S., Shim, J., Weaver, J. C., Chen, E. R., Patel, N., and Bertoldi, K., 2013, "3D Soft Metamaterials With Negative Poisson's Ratio," Adv. Mater., 25(36), pp. 5044–5049.
- [11] Kolken, H., Callens, S., Leeflang, M., Mirzaali, M., and Zadpoor, A., 2022, "Merging Strut-Based and Minimal Surface Meta-Biomaterials: Decoupling Surface Area From Mechanical Properties," Addit. Manuf., 52.
- [12] Gibson, L. J., and Ashby, M. F., 1997, Cellular Solids: Structure and Properties, 2nd ed., Cambridge University Press, Cambridge.
- [13] Lakes, R., 1987, "Foam Structures With a Negative Poisson's Ratio," Science, 235(4792), pp. 1038–1040.
- [14] Evans, K. E., 1991, "Auxetic Polymers: A New Range of Materials," Endeavour, 15(4), pp. 170–174.
- [15] Evans, K., Nkansah, M., and Hutchinson, I., 1994, "Auxetic Foams: Modelling Negative Poisson's Ratios," Acta Metall. Mater., 42(4), pp. 1289–1294.
- [16] Caddock, B. D., and Evans, K. E., 1989, "Microporous Materials With Negative Poisson's Ratios. I. Microstructure and Mechanical Properties," J. Phys. D: Appl. Phys., 22(12), pp. 1877–1882.
- [17] Evans, K. E., and Caddock, B. D., 1989, "Microporous Materials With Negative Poisson's Ratios. II. Mechanisms and Interpretation," J. Phys. D: Appl. Phys., 22(12), pp. 1883–1887.
- [18] Pham, M.-S., Liu, C., Todd, I., and Lertthanasarn, J., 2019, "Damage-Tolerant Architected Materials Inspired by Crystal Microstructure," Nature, 565(7739), pp. 305–311.
- [19] Zhang, Y., Hsieh, M.-T., and Valdevit, L., 2021, "Mechanical Performance of 3D Printed Interpenetrating Phase Composites With Spinodal Topologies," Compos. Struct., 263.
- [20] Sajadi, S. M., Tiwary, C. S., Rahmati, A. H., Eichmann, S. L., Thaemlitz, C. J., Salpekar, D., Puthirath, A. B., Boul, P. J., Rahman, M. M., Meiyazhagan, A., and Ajayan, P. M., 2021, "Deformation Resilient Cement Structures Using 3D-Printed Molds," iScience, 24.
- [21] Tao, Z., Ren, X., Sun, L., Zhang, Y., Jiang, W., Zhao, A. G., and Xie, Y. M., 2022, "A Novel Re-Entrant Honeycomb Metamaterial With Tunable Bandgap," Smart Mater. Struct., 31(095024).
- [22] Pasini, C., Inverardi, N., Battini, D., Scalet, G., Marconi, S., Auricchio, F., and Pandini, S., 2022, "Experimental Investigation and Modeling of the Temperature Memory Effect in a 4D-Printed Auxetic Structure," Smart Mater. Struct., 31(095021).
- [23] Zhan, C., Li, M., McCoy, R., Zhao, L., and Lu, W., 2022, "3D Printed Hierarchical Re-Entrant Honeycombs: Enhanced Mechanical Properties and the Underlying Deformation Mechanisms," Compos. Struct., 290.
- [24] Rayneau-Kirkhope, D., 2018, "Stiff Auxetics: Hierarchy as a Route to Stiff, Strong Lattice Based Auxetic Meta-Materials," Sci. Rep., 8(12437).
- [25] Mousanezhad, D., Babaee, S., Ebrahimi, H., Ghosh, R., Hamouda, A. S., Bertoldi, K., and Vaziri, A., 2016, "Hierarchical Honeycomb Auxetic Metamaterials," Sci. Rep., 5.
- [26] Meza, L. R., Zelhofer, A. J., Clarke, N., Mateos, A. J., Kochmann, D. M., and Greer, J. R., 2015, "Resilient 3D Hierarchical Architected Metamaterials," Proc. Natl. Acad. Sci. U. S. A., 112(37), pp. 11502–11507.
- [27] Lakes, R. S., 2017, "Negative-Poisson's-Ratio Materials: Auxetic Solids," Ann. Rev. Mater. Res., 47(1), pp. 63–81.
- [28] Kolken, H. A., and Zadpoor, A. A., 2017, "Auxetic Mechanical Metamaterials," RSC Adv., 7(9), pp. 5111–5129.
- [29] Bertoldi, K., Reis, P. M., Willshaw, S., and Mullin, T., 2010, "Negative Poisson's Ratio Behavior Induced by an Elastic Instability," Adv. Mater., 22(3), pp. 361– 366
- [30] Zhou, Y., Li, Y., Jiang, D., Chen, Y., Min Xie, Y., and Jia, L.-J., 2022, "In-Plane Impact Behavior of 3D-Printed Auxetic Stainless Honeycombs," Eng. Struct., 266.

- [31] Li, T., Hu, X., Chen, Y., and Wang, L., 2017, "Harnessing Out-of-Plane Deformation to Design 3D Architected Lattice Metamaterials With Tunable Poisson's Ratio," Sci. Rep., 7(1), p. 8949.
- [32] Box, F., Johnson, C. G., and Pihler-Puzović, D., 2020, "Hard Auxetic Metamaterials," Extr. Mech. Lett., 40.
- [33] Yousuf, M. H., Abuzaid, W., and Alkhader, M., 2020, "4D Printed Auxetic Structures With Tunable Mechanical Properties," Addit. Manuf., 35.
- [34] Jiang, Y., and Li, Y., 2018, "3D Printed Auxetic Mechanical Metamaterial With Chiral Cells and Re-Entrant Cores," Sci. Rep., 8(2397).
- [35] Wang, X.-T., Wang, B., Li, X.-W., and Ma, L., 2017, "Mechanical Properties of 3D Re-Entrant Auxetic Cellular Structures," Int. J. Mech. Sci., 131–132, pp. 396–407.
- [36] Bronder, S., Herter, F., Röhrig, A., Bähre, D., and Jung, A., 2022, "Design Study for Multifunctional 3D Re-Entrant Auxetics," Adv. Eng. Mater., 24.
- [37] Ren, X., Shen, J., Ghaedizadeh, A., Tian, H., and Min Xie, Y., 2015, "Experiments and Parametric Studies on 3D Metallic Auxetic Metamaterials With Tuneable Mechanical Properties," Smart Mater. Struct., 24.
- [38] Lohmuller, P., Favre, J., Kenzari, S., Piotrowski, B., Peltier, L., and Laheurte, P., 2019, "Architectural Effect on 3D Elastic Properties and Anisotropy of Cubic Lattice Structures," Mater. Des., 182.
- [39] Kadic, M., Milton, G. W., van Hecke, M., and Wegener, M., 2019, "3D Metamaterials," Nat. Rev. Phys., 1(3), pp. 198–210.
- [40] Meza, L. R., Phlipot, G. P., Portela, C. M., Maggi, A., Montemayor, L. C., Comella, A., Kochmann, D. M., and Greer, J. R., 2017, "Reexamining the Mechanical Property Space of Three-Dimensional Lattice Architectures," Acta Mater., 140, pp. 424–432.
- [41] Zheng, X., Lee, H., Weisgraber, T. H., Shusteff, M., DeOtte, J., Duoss, E. B., Kuntz, J. D., et al., 2014, "Ultralight, Ultrastiff Mechanical Metamaterials," Science, 344(6190), pp. 1373–1377.
- [42] Schaedler, T. A., Jacobsen, A. J., Torrents, A., Sorensen, A. E., Lian, J., Greer, J. R., Valdevit, L., and Carter, W. B., 2011, "Ultralight Metallic Microlattices," Science, 334(6058), pp. 962–965.
- [43] Vyatskikh, A., Delalande, S., Kudo, A., Zhang, X., Portela, C. M., and Greer, J. R., 2018, "Additive Manufacturing of 3D Nano-Architected Metals," Nat. Commun., 9(1), p. 593.
- [44] Roach, A. M., White, B. C., Garland, A., Jared, B. H., Carroll, J. D., and Boyce, B. L., 2020, "Size-Dependent Stochastic Tensile Properties in Additively Manufactured 316L Stainless Steel," Addit. Manuf., 32.
- [45] Jensen, S. C., Koepke, J. R., Saiz, D. J., Heiden, M. J., Carroll, J. D., Boyce, B. L., and Jared, B. H., 2022, "Optimization of Stochastic Feature Properties in Laser Powder Bed Fusion," Addit. Manuf., 56.
- [46] Liu, L., Kamm, P., García-Moreno, F., Banhart, J., and Pasini, D., 2017, "Elastic and Failure Response of Imperfect Three-Dimensional Metallic Lattices: The Role of Geometric Defects Induced by Selective Laser Melting," J. Mech. Phys. Solids., 107, pp. 160–184.
- [47] Gradl, P., Cervone, A., and Colonna, P., 2023, "Influence of Build Angles on Thin-Wall Geometry and Surface Texture in Laser Powder Directed Energy Deposition." Mater. Des., 234.
- [48] Tancogne-Dejean, T., Spierings, A. B., and Mohr, D., 2016, "Additively-Manufactured Metallic Micro-Lattice Materials for High Specific Energy Absorption Under Static and Dynamic Loading," Acta Mater., 116, pp. 14–28.
- [49] Bagheri, Z. S., Melancon, D., Liu, L., Johnston, R. B., and Pasini, D., 2017, "Compensation Strategy to Reduce Geometry and Mechanics Mismatches in Porous Biomaterials Built With Selective Laser Melting," J. Mech. Behav. Biomed. Mater., 70, pp. 17–27.
- [50] Simoes, M., Harris, J., Ghouse, S., Hooper, P., and McShane, G., 2022, "Process Parameter Sensitivity of the Energy Absorbing Properties of Additively Manufactured Metallic Cellular Materials," Mater. Des., 224.
- [51] Li, S., Hassanin, H., Attallah, M. M., Adkins, N. J., and Essa, K., 2016, "The Development of TiNi-Based Negative Poisson's Ratio Structure Using Selective Laser Melting," Acta Mater., 105, pp. 75–83.
- [52] Xiong, J., Gu, D., Chen, H., Dai, D., and Shi, Q., 2017, "Structural Optimization of Re-Entrant Negative Poisson's Ratio Structure Fabricated by Selective Laser Melting," Mater. Des., 120, pp. 307–316.
- [53] Chen, D., Li, D., Pan, K., Gao, S., Wang, B., Sun, M., Zhao, C., Liu, X., and Li, N., 2022, "Strength Enhancement and Modulus Modulation in Auxetic Meta-Biomaterials Produced by Selective Laser Melting," Acta Biomater., 153, pp. 596–613.
- [54] Carneiro, V., Puga, H., and Meireles, J., 2019, "Positive, Zero and Negative Poisson's Ratio Non-Stochastic Metallic Cellular Solids: Dependence Between Static and Dynamic Mechanical Properties," Compos. Struct., 226.
- [55] Yang, L., Cormier, D., West, H., Harrysson, O., and Knowlson, K., 2012, "Non-Stochastic Ti-6Al-4V Foam Structures With Negative Poisson's Ratio," Mater. Sci. Eng. A, 558, pp. 579–585.
- [56] Yang, L., Harrysson, O., West, H., and Cormier, D., 2015, "Mechanical Properties of 3D Re-Entrant Honeycomb Auxetic Structures Realized Via Additive Manufacturing," Int. J. Solids Struct., 69–70, pp. 475–490.
- [57] Mercer, C., Speck, T., Lee, J., Balint, D. S., and Thielen, M., 2022, "Effects of Geometry and Boundary Constraint on the Stiffness and Negative Poisson's Ratio Behaviour of Auxetic Metamaterials Under Quasi-Static and Impact Loading," Int. J. Impact Eng., 169.

- [58] Geng, L., Wu, W., Sun, L., and Fang, D., 2019, "Damage Characterizations and Simulation of Selective Laser Melting Fabricated 3D Re-Entrant Lattices Based on In-Situ CT Testing and Geometric Reconstruction," Int. J. Mech. Sci., 157– 158, pp. 231–242.
- [59] Schwerdtfeger, J., Heinl, P., Singer, R. F., and Körner, C., 2010, "Auxetic Cellular Structures Through Selective Electron-Beam Melting," Phys. Status Solidi (b), 247(2), pp. 269–272.
- [60] Teng, X. C., Ren, X., Zhang, Y., Jiang, W., Pan, Y., Zhang, X. G., Zhang, X. Y., and Xie, Y. M., 2022, "A Simple 3D Re-Entrant Auxetic Metamaterial With Enhanced Energy Absorption," Int. J. Mech. Sci., 229.
- [61] Suard, M., Martin, G., Lhuissier, P., Dendievel, R., Vignat, F., Blandin, J.-J., and Villeneuve, F., 2015, "Mechanical Equivalent Diameter of Single Struts for the Stiffness Prediction of Lattice Structures Produced by Electron Beam Melting," Addit. Manuf., 8, pp. 124–131.
- [62] Photiou, D., Avraam, S., Sillani, F., Verga, F., Jay, O., and Papadakis, L., 2021, "Experimental and Numerical Analysis of 3D Printed Polymer Tetra-Petal Auxetic Structures Under Compression," Appl. Sci., 11.
- [63] Chen, Y., and Fu, M.-H., 2017, "A Novel Three-Dimensional Auxetic Lattice Meta-Material With Enhanced Stiffness," Smart Mater. Struct., 26(105029).
- [64] Shokri Rad, M., Prawoto, Y., and Ahmad, Z., 2014, "Analytical Solution and Finite Element Approach to the 3D Re-Entrant Structures of Auxetic Materials," Mech. Mater., 74, pp. 76–87.
- [65] Shokri Rad, M., Ahmad, Z., and Alias, A., 2015, "Computational Approach in Formulating Mechanical Characteristics of 3D Star Honeycomb Auxetic Structure," Adv. Mater. Sci. Eng., 2015, pp. 1–11.
- [66] Lvov, V., Senatov, F., Korsunsky, A., and Salimon, A., 2020, "Design and Mechanical Properties of 3D-Printed Auxetic Honeycomb Structure," Mater. Today Commun., 24.
- [67] Lvov, V., Senatov, F., Stepashkin, A., Veveris, A., Pavlov, M., and Komissarov, A., 2020, "Low-Cycle Fatigue Behavior of 3D-Printed Metallic Auxetic Structure," Mater. Today: Proc., 33, pp. 1979–1983.
- [68] Lim, T.-C., 2016, "A 3D Auxetic Material Based on Intersecting Double Arrowheads: A 3D Auxetic Material Based on Intersecting Double Arrowheads," Phys. Status Solidi (b), 253(7), pp. 1252–1260.
- [69] Zheng-Dong, M., 2010, Three-Dimensional Auxetic Structures and Applications Thereof, US PATENT US 2010/0119792A1.
- [70] Zhang, M., 2021, "Study of Auxetic Composite With Isotropic Poisson's Ratio by Random Inclusions," Ph.D. Dissertation, Hong Kong Polytechnic University.
- [71] Álvarez Elipe, J. C., and Díaz Lantada, A., 2012, "Comparative Study of Auxetic Geometries by Means of Computer-Aided Design and Engineering," Smart Mater. Struct., 21.
- [72] Zhang, W., Li, Z., Wang, J., Scarpa, F., and Wang, X., 2022, "Mechanics of Novel Asymmetrical Re-Entrant Metamaterials and Metastructures," Compos. Struct., 291.
- [73] Dassault Systémes SIMULIA Abaqus/Standard CAE 2023, November 2022.
- [74] Yang, Q.-S., and Becker, W., 2004, "Numerical Investigation for Stress, Strain and Energy Homogenization of Orthotropic Composite With Periodic Microstructure and Non-Symmetric Inclusions," Comput. Mater. Sci., 31(1–2), pp. 169–180.
- [75] ASTM Standard C109/C109M-23. Test Method for Compressive Strength of Hydraulic Cement Mortars (Using 2-in. or [50mm] cube specimens).
- [76] Robert McNeel and Associates (TLM, Inc.), Rhino 3D v7, November, 2020.
- [77] Dassault Systémes, Solidworks 3D CAD Design 2023, September 2022.
- [78] Materialise NV, Magics 19, October, 2014.
- [79] EOS Gmbh, EOSPrint 2, December, 2020.
- [80] Gross, A., Pantidis, P., Bertoldi, K., and Gerasimidis, S., 2019, "Correlation Between Topology and Elastic Properties of Imperfect Truss-Lattice Materials," J. Mech. Phys. Solids, 124, pp. 577–598.
- [81] Object Research Systems (ORS) Inc., Dragonfly Pro 2022.2, 2022.
- [82] Martin, A. A., Calta, N. P., Khairallah, S. A., Wang, J., Depond, P. J., Fong, A. Y., Thampy, V., et al., 2019, "Dynamics of Pore Formation During Laser Powder Bed Fusion Additive Manufacturing," Nat. Commun., 10(1), p. 1987.
- [83] Huang, Y., Fleming, T. G., Clark, S. J., Marussi, S., Fezzaa, K., Thiyagalingam, J., Leung, C. L. A., and Lee, P. D., 2022, "Keyhole Fluctuation and Pore Formation Mechanisms During Laser Powder Bed Fusion Additive Manufacturing," Nat. Commun., 13(1), p. 1170.
- [84] Kan, W. H., Chiu, L. N. S., Lim, C. V. S., Zhu, Y., Tian, Y., Jiang, D., and Huang, A., 2022, "A Critical Review on the Effects of Process-Induced Porosity on the Mechanical Properties of Alloys Fabricated by Laser Powder Bed Fusion," J. Mater. Sci., 57(21), pp. 9818–9865.
- [85] ASTM Standard E83-16. Practice for Verification and Classification of Extensometer Systems.
- [86] Pijpers, R., and Slot, H., 2020, "Friction Coefficients for Steel to Steel Contact Surfaces in Air and Seawater," J. Phys.: Conf. Series, 1669(1), p. 012002.
- [87] Mirabal, A., Loza-Hernandez, I., Clark, C., Hooks, D. E., McBride, M., and Stull, J. A., 2023, "Roughness Measurements Across Topographically Varied Additively Manufactured Metal Surfaces," Addit. Manuf., 69.
- [88] Tancogne-Dejean, T., and Mohr, D., 2018, "Stiffness and Specific Energy Absorption of Additively-Manufactured Metallic BCC Metamaterials Composed of Tapered Beams," Int. J. Mech. Sci., 141, pp. 101–116.